Direct visualization of emergent metastatic features within an *ex vivo* model of the tumor microenvironment

Libi Anandi, Jeremy Garcia, Manon Ros, Libuše Janská, Josephine Liu, Carlos Carmona-Fontaine*

Center for Genomics & Systems Biology, Department of Biology, New York University, New York, NY 10003, USA

*Correspondence: cf97@nyu.edu

ABSTRACT

Preventing tumors from acquiring metastatic properties would dramatically reduce cancer mortality[1–4]. The emergence of metastatic cells is promoted by interactions with stromal cells under environmental conditions such as hypoxia and nutrient-deprivation[5–11]. Unfortunately, these conditions arise deep within tumor tissues – afar from the vasculature – and thus the observation of nascent metastases has been exceedingly challenging. We present an *ex vivo* model of the tumor microenvironment that enables the observation of tumor cells in their native 3D context with high spatial and temporal resolution. In this system, called 3MIC, tumor cells spontaneously create ischemic conditions so we can study how they impact the emergence of pro-metastatic features. Consistent with previous experimental and clinical data, we showed that ischemic-like conditions in the 3MIC increase cell migration and invasion in tumor spheroids formed from a panel of established and freshly derived tumor lines. The 3MIC allowed us to precisely observe when these pro-metastatic features emerge, to track ischemic cells with single cell resolution, and to directly observe how these cell behaviors change upon interactions with stromal cells. We used the 3MIC to observe the effects of drugs targeting cell migration and we found evidence that ischemic cells acquire resistance to paclitaxel. Overall, the 3MIC allows us to directly observe the emergence of metastatic tumor features in a physiologically relevant model of the tumor microenvironment. This simple and cost-effective system can dissect the complexity of the tumor microenvironment to test perturbations that may prevent tumors from becoming metastatic.

INTRODUCTION

Most cancer fatalities are directly or indirectly caused by metastases[4]. Thus, treating pre-metastatic tumor cells before they acquire migratory and invasive properties could dramatically reduce cancer mortality[12]. While later metastatic steps can be studied using circulating tumor cells, biopsies, and *postmortem* analysis of metastases[13,14], nascent metastases are harder to model and to detect.

The conditions that induce metastasis in the primary tumor remain poorly understood. For example, when or where a metastatic clone emerges is unpredictable[15–18], and thus particularly difficult to observe *in vivo*[18–20]. The intricacies of this process can hamper the identification of key potential therapeutic targets[21,22]. In addition, most murine tumor models are better at recapitulating primary tumor growth than later stages of the disease and can be prohibitively expensive[23,24]. Thus, studying and visualizing the initial steps of metastasis *in vivo* has been incredibly challenging. Cell cultures on the other hand, cannot capture the systemic nature of the multiple steps involved along the metastatic process[20]. However, the recreation *in vitro* or *ex vivo* of the initial conditions that allow metastases to emerge, may be more feasible. Still, these initial steps remain hard to model as they are triggered by a combination of cell-autonomous factors – such as oncogenic mutations – and environmental signals such as hypoxia and cell-cell interractions[7,10,25,26].

We sought to develop a cell culture system capable of recreating the initial conditions in which metastases emerge. First, we wanted to capture the complex metabolic microenvironment of solid tumors – a known key factor in metastasis initiation[27–29]. While hypoxia is a common feature of solid tumors, it rarely – if ever – occurs alone. In solid tumors, cells close to blood vessels are well-nurtured. As nutrients and oxygen diffuse inside the tumor mass, resources in the microenvironment become progressively scarcer while metabolic by-products, such as lactic acid, accumulate[30–37]. It is now recognized that it is the complex combination of factors in these poorly perfused or ischemic environments, rather than hypoxia alone, what drives the emergence of metastasis[5,6,8,38]. Since these ischemic conditions arise deep within tumors, accessing and observing the emergence of metastatic cells has been virtually impossible.

Second, we needed where tumors can easily interact with other cells. Tumor infiltrated immune and stromal cells are also key in the regulation of metastasis[9–11]. For example, recent *in vivo* imaging evidence shows that tumor-associated macrophages activate invasion in disseminating tumor cells[39]. Recent advances in organoid biology are allowing the formation of *ex vivo* tumor-like structures where therapies can be tested on patient-derived samples with complex cellular compositions[40–43]. Still, the inaccessibility of ischemic tumor cells makes imaging tumor-stromal interactions an almost insurmountable challenge.

Considering these two goals, we developed an *ex vivo* model of the tumor microenvironment designed to visualize the transition from poorly motile primary tumor cells to migratory metastatic-like cells. Our 3D Microenvironmental Chamber or 3MIC, incorporates key tumor features such as the infiltration of immune cells and the spontaneous formation of metabolic gradients that mimic tumor ischemia and other conditions within the tumors. Importantly, due to its unique geometry, the 3MIC allows the imaging of ischemic cells with ease and with unprecedented temporal and spatial resolution. To illustrate the features of the 3MIC, we showed that oxygen and nutrient poor-environments directly drive the emergence of metastatic features such as increased cell migration, degradation of the extracellular matrix (ECM), and loss of epithelial features. Combining *in vivo* experiments with 3MIC cultures, we showed that these changes were reversible suggesting that metastatic features can arise even in the absence of clonal selection by hypoxia or other environmental challenges. We also showed tumor interactions with stromal cells such as macrophages and endothelial cells, increases the pro-metastatic effects of ischemia. Finally, we demonstrate how the 3MIC can be used to test how drug effects may change according to local metabolic conditions. In all, the 3MIC is an affordable cell culture system where different components of the tumor microenvironment – and their effect on the first steps of metastasis – can be carefully dissected. Its amenability for live imaging can complement *in vivo* studies to better understand and treat the emergence of metastases.

RESULTS

A 3D *ex vivo* model for the direct visualization of ischemic tumor cells

Visualizing ischemic cancer cells present a unique challenge as they are located deep within tumors and the same is true in typical *ex vivo* cultures including organoids (Fig. 1A). We recently developed the **Me**tabolic **Mi**croenvironment **C**hamber (MEMIC), an *ex vivo* culture system where a cell monolayer generates spatial gradients of metabolites that mimic tumor ischemia[35–37]. Importantly, cells growing in ischemic-like conditions within the MEMIC are as easy to image as well-nurtured cells[44,45]. We thus thought that this system may be ideal to study the impact of the metabolic microenvironment on tumor cell migration. The MEMIC has only been used in 2D cultures, so we first needed to verify the formation of ischemic-like gradients in 3D cultures. We thus expressed a fluorescent hypoxia sensor (5xHRE-GFP[44]) in a panel of epithelial tumor cells also expressing constitutive plasma membrane fluorescence (mCherry-CAAX[44]). We then aggregated these cells into small tumor spheroids and cultured them in the MEMIC embedded in a collagen and laminin-rich ECM scaffolds. In our previous reports, 2D cell monolayers in the MEMIC show signs of hypoxia after less than 24h. However, even after 48 hours of culture we were unable to detect signs of hypoxia in tumor spheroids (Fig. S1A).

Cell density is crucial for the formation of metabolite gradients in the MEMIC[44]. A typical 2D MEMIC culture has ~10^5 cells – which is approximately 100 times higher than the total cell number that we used in our 3D cultures. Thus, it is possible that the lack of hypoxia in these experiments was due to low cell density. Attempts to increase total cell number by adding more tumor spheroids, resulted in large cell masses due to the fusion of neighboring clusters which impeded the detailed examination of ischemic cells. We thus concluded that the MEMIC was inadequate to study the impacts of the metabolic microenvironment on 3D cultures.

We decided to develop a new culture system specifically designed for 3D multicellular tumor structures. We named this new system the **3**D **mi**croenvironment **c**hamber (3MIC). The principle behind the 3MIC is similar to the MEMIC: a dense monolayer of cells is restricted from accessing nutrients and oxygen from all but one side. This side is open to a large volume of fresh media and thus acts as a nutrient and oxygen source while cells act as a resource sink. In the 3MIC however, these cells are not the focus of our analyses and only act as nutrient and

104 oxygen consumers. These “consumer cells” grow up-side-down on a coverslip at the top of the
105 chamber. We then embedded tumor spheroids on ECM and grew them underneath consumer
106 cells. The location of consumer cells on top is designed to have tumor spheroids closer to the
107 objective of an inverted microscope (Fig. S1B). Importantly, this two-tier system allows us to
108 have spheroids at a low density but exposed to metabolic gradients generated by consumer
109 cells growing directly above them (Fig. 1B; Fig. S1B).

110 We first confirmed that consumer cells form metabolic gradients. As in our MEMIC experiments,
111 we seeded a monolayer of cells derived from a mouse model of lung adenocarcinoma driven by
112 $KRAS^{G12D}$ and loss of TP53[46] (Lung KP cells) expressing 5xHRE-GFP and mCherry-CAAX. As
113 expected, these cells displayed a strong gradient of GFP that increased with the distance to the
114 opening of the 3MIC (Fig. S1C). We then tested whether these gradients could influence tumor
115 spheroids growing below consumer cells, by adding ECM-embedded spheroids to 3MICs with or
116 without consumer cells. As in our previous MEMIC experiment, spheroids in control 3MICs
117 without consumers did not show signs of hypoxia (Fig. 1C,D). In contrast, distal tumor spheroids
118 growing in 3MICs with consumer cells showed levels of the GFP hypoxia reporter, while
119 fluorescence levels in well-nurtured/proximal spheroids were negligible. We obtained similar
120 results with three independently derived clones of Lung KP cells and in experiments using
121 different cell lines and with a different hypoxia reporter[47] (Fig. S1D). Overall, these results show
122 that consumer cells in the 3MIC form ischemic gradients that can influence the local metabolic
123 microenvironment experienced by neighboring tumor spheroids. As changes in the metabolic
124 microenvironment of the 3MIC occur perpendicular to our imaging path, we can observe how
125 these conditions affect tumor structures – ischemic and well-nurtured – with unprecedented
126 spatial and temporal resolution.

127 **Hypoxia is required but not sufficient to increase invasive features in tumor spheroids**

128 In the experiments described above we also observed dramatic morphological changes along
129 the ischemia gradient. Spheroids close to the opening had a modest size increase and
130 remained smooth and mostly rounded. In contrast, distal ischemic spheroids acquired a ruffled
131 and protrusive morphology expanding significantly in volume (Fig. 1E,F; Video S1). Hypoxia is
132 critical in the induction of pro-metastatic tumor features but we speculated that additional

133 metabolic conditions in the 3MIC – such as nutrient deprivation and lactic acid accumulation –
134 may increase tumor cell migration and invasion. To compare the effects of different conditions
135 on spheroid's morphology, we defined *invasiveness index* as the inverse of their circularity. This
136 index will increase in more spheroids with more irregular and protrusive shapes and remain
137 small in smoother and cell structures (Fig. 1G).

138 We first tested whether hypoxia was *sufficient* to trigger morphological changes and increase
139 cell migration in 3D tumor spheroids. We compared spheroids cultured in regular petri dishes
140 incubated under different oxygen tensions (21% and 1%) with spheroids cultured in the 3MIC.
141 Tumor spheroids cultured in a hypoxic incubator increased levels of the GFP-based hypoxia
142 sensor to levels comparable to ischemic clusters in the 3MIC (Fig. S1E). Hypoxic spheroids
143 however were not as invasive as spheroids in the 3MIC and were only slightly more invasive
144 than spheroids cultured in regular incubators (Fig. 1G). These results show that hypoxia alone
145 triggers relatively minor morphological changes and cannot fully recapitulate the changes that
146 we observe in ischemic regions of the 3MIC.

147 We then tested whether hypoxia was *required* in altering spheroid morphologies, we took
148 advantage of the selective permeability of polydimethylsiloxane (PDMS)[44,45,48]. PDMS is
149 permeable to oxygen and other gases, but not to soluble metabolites. We thus constructed
150 3MICs using a PDMS membrane molded into the shape of a glass coverslip. In these modified
151 3MICs, cells form gradients of nutrients and metabolic byproducts, but oxygen rapidly
152 equilibrates across the PDMS membrane and thus there is no hypoxia (Fig. S1F). In this
153 scenario, the effect of consumer cells was minimal, with only small changes in the morphology
154 of spheroids (Fig. 1H; Fig. S1F). Altogether, these results show that hypoxia is *required* but not
155 *sufficient* to increase the morphological changes we observed in ischemic tumor spheroids. In
156 addition, these results highlight the advantage to consider complex metabolic challenges
157 instead of single parameters such as hypoxia.

158 **Ischemia stimulates persistent cell migration**

159 The morphological changes described above seemed to be conserved as we observed similar
160 changes in a panel of cell lines (Fig. S2A,B). As expected, this increase in size was not driven
161 by cell proliferation. Overall, we detected a small number of proliferating cells in fixed spheroids

162 (via phospho-H3 immunostaining, Fig. S2C) or using FUCCI-based live imaging cell cycle
163 reporters (Fig. S2D; Video S2). Furthermore, live imaging analyses revealed a significant
164 decrease in the local cell density of ischemic clusters (Fig. 2A; Video S3)[48] – suggesting that the
165 expansion of ischemic spheroids may arise from increased cell dispersion rather than growth
166 (Fig. 2B).

167 Taking advantage of the high temporal and spatial resolution in live microscopy afforded by the
168 3MIC, we measured the migratory properties of individual tumor cells. To allow for accurate
169 automated cell tracking, we modified Lung KP cells to express a nuclear fluorescent protein
170 (H2B-YFP). We then formed chimeric spheroids of these cells with isogenic Lung KP cells
171 expressing a different fluorophore (mCherry-CAAX; Fig. 2C; Video S4). We tracked hundreds of
172 cells from different spheroids along the gradient of ischemia. Analysis of nearly 900 tracks of
173 individual cells showed a large heterogeneity in their motility as some cells wandered near their
174 origin, while others moved large distances from their origin. On average however, cells from
175 ischemic clusters travelled further from their original location than cells from well-nurtured
176 clusters (Fig. 2D, Fig. S2E,F; Video S4). This increase in net displacement in ischemic cells was
177 not due to an increase in speed (Fig. S2G) but rather because they move more persistently than
178 well-nurtured cells (Fig, 2E). Consistent with their increased persistence, the movement of
179 ischemic cells was *superdiffusive – i.e.* significantly more directional than expected by a random
180 walk[49] (Fig. 2F, **m**ean **s**quare **d**isplacement (MSD) constant, σ=1.19; Fig. S2G). In contrast,
181 MSD analysis of cells in well-nurtured clusters was indistinguishable from a random walk (Fig.
182 2F, MSD constant, σ=1.02).

183 To further explore these data, we defined *runners* as cells whose net displacement was greater
184 than an arbitrary distance threshold (50μm). At most values of this threshold, ischemic clusters
185 had about twice as many runners than well-nurtured spheroids or spheroids in chambers
186 without consumer cells. Interestingly, we observed a directional bias in the movement of runner
187 cells away from ischemia as if they were moving toward nutrient sources (Fig. 2G; Fig. S2H).
188 However, this directional bias was small and only significant under some definitions (distance
189 thresholds) of runner cells (Fig. S2I). We thus concluded that, in this setting, metabolite
190 gradients do not act as significant orientation cues. Still, our data shows that ischemia leads to

191 more persistent movements in three-dimensional tumor cultures resulting in highly dispersive
192 and invasive tumor spheroids.

193 **Ischemic tumor cells lose epithelial features and increase ECM degradation**

194 We then sought to determine which changes were specifically triggered by ischemia. Our cell
195 tracking analyses showed that changes at the individual cell level – such as cell speed and
196 cellular interactions – such cell-cell and cell-ECM adhesions – were modulated by ischemia.

197 The MSD increase in ischemic cells suggests that their movements are less constrained by
198 surrounding obstacles[50]. Typically, cell movements are constrained by the ECM or by adhesion
199 to other cells[42,43]. Consistently, hypoxic tumor cells are known to increase ECM invasion[7,51] and
200 to have lower levels of epithelial cell adhesion molecules such as E-Cadherin (E-Cad)[52–58]. We
201 thus wanted to validate whether ischemic spheroids increase ECM degradation and reduce cell-
202 cell adhesion in the 3MIC. To measure ECM degradation, we first used an assay where ECM
203 proteins are laid over a coverslip coated with fluorescent gelatin[59]. More invasive clusters will
204 break down the ECM network, and eventually degrading the labeled gelatin resulting in local
205 loss of fluorescence (Fig. 3A; Fig. S3A). As an orthogonal approach, we cultured tumor
206 spheroids in DQ-Collagen – a labeled but quenched form of collagen that fluoresces when
207 cleaved[60]. In both assays, ischemic clusters showed significantly higher levels of ECM
208 degradation (Fig. S3B) with foci of ECM degradation colocalizing with more invasive spheroid
209 regions (Fig. S3C).

210 Hypoxia in the tumor microenvironment is known to decrease epithelial features such as E-Cad
211 levels in carcinomas and we have previously recapitulated that effect in the MEMIC[44].
212 Consistent with these previous data, immunofluorescent analysis of ischemic spheroids in the
213 3MIC showed a dramatic decrease in E-Cad levels instead of their usual well-defined cell-cell
214 adhesions lined by high levels of E-Cad (Fig. 3C,D). We observed a similar trend using a
215 fluorescent E-Cad live reporter (Fig. S3D). Interestingly, these cells also express mesenchymal
216 markers such as vimentin, but we did not observe significant changes in the levels of this
217 protein (Fig. S3E). Taken together, these results show that ischemic cells decrease epithelial
218 adhesion and degrade their surrounding ECM more efficiently than their well-nurtured
219 counterparts.

220 **A model of persistent tumor migration in the absence of directional cues**

221 Our results are consistent with well-established evidence that tumor hypoxia, *i.e.* ischemia,
222 increase migratory and invasive cell abilities[11,15,17,20]. However, since ischemic conditions arise
223 deep within tumors, these cells must move long distances within the tumor to eventually reach
224 the bloodstream. As we hinted before, an appealing hypothesis is that nutrients or oxygen act
225 as directional cues that orient the movements of ischemic cells. However, we did not find strong
226 evidence in our data to support this hypothesis (Fig. 2G; Fig. S2H-I). We thus asked whether a
227 simple decrease in epithelial adhesion and an increase in ECM invasion can recapitulate our
228 experimental observations and provide a model of how ischemic cells escape from poor
229 conditions *in vivo*.

230 We decided to address this question using a Cellular Potts Model (CPM)[61,62]. CPMs are a
231 computational framework frequently used to model problems of differential cell adhesion and
232 cell sorting in morphological processes[63]. In CPMs, any number of 'cell types' exist on a grid
233 and have different affinities for each other and for their surrounding substrate. In CPMs, high
234 affinity contacts have a lower surface energy and thus they are more stable. In contrast, low
235 cell-cell or cell-substrate affinities are represented as highly energetic and unstable contacts At
236 every simulated time point or Monte Carlo Step (MCS), the CPM tries to minimize the energy of
237 the system resulting in changes in cell shape, localization, etc. according to local energy
238 levels[61,62]. Our modeled tumors were formed by two cell types: *core* (ischemic) and *cortical*
239 (well-perfused) cells according to their positions at the beginning of the simulation. Our specific
240 goal was to test whether changes in cell-cell and cell-substrate adhesion would allow core cells
241 to move through cortical cells and eventually invade into the surrounding ECM.

242 We modelled the reduced levels of E-Cad we observed in ischemic cells as an increase in the
243 surface energy between core cells (decreasing their stability). Energy levels were set to ensure
244 that the adhesion between core cells was low, between cortical cells was high, and intermediate
245 between the two cell types. We tested a range of affinity parameters obtaining similar qualitative
246 results as long as we kept these relationships (Fig. 3E; see additional details in Tables S1 and
247 S2). Implementation of these changes resulted in clusters where core cells mixed with cortical
248 cells but there was no invasion into their surroundings (Fig. 3F; Video S5). To model the
249 increased ECM invasion in ischemic cells, we set the affinity for the surrounding ECM to be

250 higher in core than in cortical cells. This feature alone, produced poor mixing between
251 populations and a moderate trend to invade the ECM (Fig. 3F; Video S5). However, cell
252 movements were random and did not show the persistent movements observed in our
253 experimental data (Fig. 3F; S3F).

254 The combination of these two rules – core cells with decreased cell-cell adhesion but increased
255 affinity for the ECM – produced the most interesting outcomes. Ischemic core cells moved
256 through layers of well-perfused cells and rapidly dispersed through the surrounding ECM (Fig.
257 3F; Video S5). These virtual cell movements were remarkably close to the movements of our
258 experimental cells. For example, tracks of core and cortical cells in the model (Fig. 3G),
259 resembled the movements of ischemic and well-nurtured cells, respectively (compare with Fig.
260 S2F). Most strikingly, the MSD of core cells in this scenario displayed increased by the same
261 order of magnitude as in our experimental cells in the 3MIC (compare Fig. 3H and Fig. 2F).
262 Altogether these data suggest that increasing the affinity for the ECM and decreasing cell-cell
263 adhesion is sufficient for the spontaneous emergence of directional movements and the
264 dispersion of core cells into distal ECM surroundings – even in the absence of explicit
265 directional cues. While it is likely that many other mechanisms contribute to the translocation of
266 hypoxic tumor cells to regions from where they can spread from, this model proposes a minimal
267 set of conditions that can facilitate this process.

268 **Pro-metastatic features induced by ischemia are reversible**

269 Hypoxic and ischemic environments can select for more aggressive and metastatic clones[5,64,65].
270 The contribution of clonal selection in our brief 3MIC experiments (~24-72h) is negligible. *In vivo*
271 however, time scales are much longer, which may allow ischemia to select for more migratory
272 clones. We hypothesized that if ischemic cells are selected to be more migratory *in vivo*, they
273 should display a higher migratory phenotype in the 3MICs – irrespective of their location along
274 the ischemic gradient. We thus injected Lung KP expressing GFP-HRE cells into the flank of
275 syngeneic mice and after 2 weeks, we extracted these tumors and dissociated them into single
276 cells. Using flow cytometry, we sorted ischemic from non-ischemic cells according to their GFP
277 levels (Fig. S4A). From these sorted cells, we generated tumor spheroids, which we then
278 cultured into separated 3MICs (Fig. 4A; Fig. S4B). As shown in figure 4C, the increase in cell

279 migration and invasion strongly correlated with the distance to the opening but whether
280 spheroids came from hypoxic and non-hypoxic tumor regions (Fig. 4B,C). Importantly, these
281 spheroids did not show any increase in migratory properties when cultured in 3MICs without
282 consumers – regardless of where in the tumor they came from (Fig. S4C,D). Altogether, these
283 results show that, at least in this system, the pro-metastatic features produced by ischemia are
284 phenotypic changes that do not require clonal selection.

285 **Reconstruction and visualization of more complex microenvironments**

286 Solid tumors are infiltrated with a variety of stromal and immune cells[9–11]. Tumor-associated
287 macrophages (TAMs) are one of the most abundant cell types in solid tumors and can increase
288 cancer progression, metastasis, and mortality[11,66–71]. TAMs can recruit endothelial cells helping
289 to orchestrate the vascularization process required for tumor growth and metastasis. We
290 recently showed that a combination of hypoxia and high lactic acid, activate the ERK/MAPK in
291 macrophages who then secrete VEGFA and induce tube-like morphogenesis in endothelial
292 cells[45]. To test whether we could recapitulate these data in the 3MIC, we generated endothelial
293 clusters from SVEC4-10 cells (referred as SVECs) and co-cultured them with bone marrow-
294 derived macrophages. As controls we examined similar SVEC clusters in 3MICs without
295 macrophages. In the absence of macrophages, clusters of endothelial cells remained mostly
296 rounded, even in the presence of consumer cells and regardless of their location along the
297 ischemic gradient (Fig. 5A; Video S6). In the presence of macrophages however, ischemic
298 endothelial cells extended away from clusters and sprouted into the ECM (Fig. 5A; Video S6).
299 This tube-like morphogenesis did not occur in well-nurtured regions of the 3MIC (Fig. 5A; Video
300 S6). In the absence of consumer cells SVEC clusters did not show major morphological
301 changes (Fig. S5A). In addition, inhibition of VEGF signaling completely abrogated
302 macrophage-induced endothelial sprouting (Fig. 5B; Fig. S5B) confirming that ischemic – but
303 not well-nurtured – macrophages have a VEGF-dependent angiogenic role in tumors[45,66].

304 We next co-cultured tumor spheroids with macrophages. In these experiments. we observed
305 that the presence of macrophages – even in well-nurtured regions – spheroids displayed
306 increased cell migration and ECM invasion and these changes increased with ischemia (Fig.
307 5C). Similarly, macrophages and ischemia synergized to decrease E-Cad levels (Fig. 5D; Fig.

308 S3D). Live imaging of these tumor-macrophage interactions revealed a fascinating behavior:
309 tumor cells from ischemic spheroids extended protrusions towards macrophages appearing to
310 physically drag them into the tumor cell cluster (Video S7). This observation suggests that there
311 may be an understudied mechanical mechanism of macrophage infiltration of tumors.

312 Increasing the complexity of co-cultures in the 3MIC is simple. For example, we produced a
313 triple co-culture of chimeric SVEC/Lung KP spheroids grown in ECM and surrounded by
314 macrophages (Fig. 5E; Video S8). Here again we observed the strong synergy between
315 metabolic and macrophage signals in promoting morphological changes in tumor and
316 endothelial cells.

317 **Ischemic cells are more resilient to anti-migratory drugs**

318 Witnessing the transition from poorly migratory tumor cells to highly invasive ones, provides a
319 unique opportunity to test drugs that directly target metastatic initiation. As a proof of principle,
320 we tested the effects of paclitaxel on migratory tumor spheroids. Paclitaxel stabilizes
321 microtubules leading to mitotic arrest and cell death[72]. At lower concentrations however,
322 paclitaxel inhibits cell migration without a significant effect in cell viability[73,74]. At these
323 concentrations however, paclitaxel failed to inhibit the migration of ischemic cells (Fig. 6A,B).
324 The lack of response in ischemic spheroids may result from three possible mechanisms. First,
325 drug levels may decrease due to passive diffusion along the 3MIC. We quickly ruled out this
326 explanation because spheroids in control 3MICs without consumers were not resistant to
327 paclitaxel (Fig. 6A,B). Second, consumer cells may decrease drug levels by consuming or
328 actively degrading paclitaxel. To test this alternative, we needed to visualize or measure local
329 levels of paclitaxel and compare how they change along 3MICs with or without consumer cells.
330 Fortunately, fluorophore-conjugated paclitaxel analogues are routinely used as probes to label
331 microtubules. Thus, we used the intensity of microtubule staining as a proxy for the local drug
332 concentration after adding known quantities of the fluorescent paclitaxel analog (docetaxel-
333 Cy5). As shown in Fig. 6C, fluorescence levels progressively decreased in more distal
334 spheroids, but they did so at the same rate in 3MICs with or without consumer cells (Fig. 6C,D;
335 Fig. S6C). These results show that consumer cells have a negligible effect on paclitaxel

336 concentration and this mechanism cannot explain how ischemic cells become unresponsive to
337 this drug.

338 We established that concentrations ranging from 30-200nM produced a complete inhibition of
339 cell movements in well-nurtured tumor spheroids, while having a negligible effect on cell viability
340 (Fig. S6A,B).

341 Finally, ischemia may induce a true mechanism of drug resistance that cannot be explain simply
342 by lower levels of the drug. To test this hypothesis, we treated spheroids in 3MICs with
343 paclitaxel concentrations that were high enough to ensure that even the most distal spheroids
344 were exposed to drug levels that would inhibit the migration of well-nurtured clusters (~45nM at
345 10mm and ~24nM at 12mm, Fig. 6D). Even under these conditions, ischemic clusters were able
346 to increase their cell migration and invasion capabilities (Fig. S6D). We thus concluded that
347 ischemic spheroids are more resistant to paclitaxel by mechanisms beyond drug penetration
348 and diffusion (Fig. 6E).

349 Altogether these experiments show that the 3MIC recapitulates key features of the tumor
350 microenvironment. It allows for imaging ischemic cells that are hidden to conventional
351 techniques and permits testing the role of different elements of the tumor microenvironment and
352 the effects of drugs on the emergence of metastatic features.

353 **DISCUSSION**

354 Animal models are fundamental to study the complexity and heterogeneity of the tumor
355 microenvironment[24,75]. In these *in vivo* models however, it is hard to isolate and weigh the
356 contributions of different variables to tumor progression, and large experiments are prohibitively
357 expensive for most laboratories[61,62]. On the other hand, conventional *in vitro* approaches offer
358 much better experimental control and can be easily scaled up for high throughput approaches.
359 However, *in vitro* models do not usually consider the cellular and molecular heterogeneity of the
360 tumor microenvironment. The lack of models that can bridge the complexity of *in vivo* models
361 with the ease of *in vitro* cultures has impaired progress in understanding the tumor
362 microenvironment and how it can modulate the emergence of metastatic tumor features[12,21,22].
363 To bridge this technical gap, we described the design and implementation of the 3MIC – an *ex*
364 *vivo* culture system that allows visualizing the acquisition of metastatic-like migratory properties
365 in complex 3D tumor cultures.

366 The results shown here are consistent with well-established evidence that hypoxia is essential
367 for the emergence of metastasis. The 3MIC however, allowed us to gain new insights into this
368 process by 1) re-creating a complex ischemic-like metabolic microenvironment rather than
369 simple hypoxia and 2) overcoming challenges associated with imaging ischemic cells that are
370 usually located deep within tumor structures. The ischemic-like environment formed in the 3MIC
371 better mimics metabolic conditions in tumors such as accumulation of lactic acid and nutrient
372 deprivation[36,44,76]. Consistently, nutrient deprivation triggers the release of pro-migratory
373 cytokines[77] and there is accumulating evidence that cell metabolic signals can directly
374 determine the likelihood and destination of metastases[27,28].

375 Our data shows that ischemic cells display a more efficient dispersion. Consistent with previous
376 evidence[78,79], we showed here that ischemia decreases epithelial cell adhesion and increases
377 the degradation of the extracellular matrix. While some of our observations share features with
378 the process of epithelial-to-mesenchymal transition (EMT), we avoided using this term as we
379 only observed a decrease in epithelial features without significant increase in mesenchymal
380 markers such as vimentin. In addition, the contribution EMT to the metastatic process remains
381 controversial[54,80,81].

382 At the single cell level, ischemia increases cell persistence without a significant change in cell
383 polarity or increasing directional cell migration. However, we observed a small bias towards
384 higher nutrients in the direction of cell movements. While in our setting these differences were
385 not statistically significant, it would be consistent with a widespread set of examples of nutrient-
386 driven chemotaxis in prokaryotes and in other eukaryotic cells[82,83]. Interestingly, the key nutrient
387 sensor mTORC2 is critical in neutrophil chemotaxis. Still, additional experiments will be needed
388 to establish whether tumor cells can follow nutrient gradients or not.

389 Recent evidence shows that tumor hypoxia can act as an evolutionary pressure that selects for
390 tumor clones that are more resilient to stressors such as reactive oxygen species[54,64,84].
391 However, our data shows that hypoxia and ischemia can alter cells directly without the need of
392 clonal selection. These two ideas are not in conflict and our experimental conditions are not free
393 of caveats. Most likely the acquisition of metastatic features in patients occurs by a combination
394 of selection and opportunistic adaptations to the tumor microenvironment.

395 The direct visualization of tumor-stroma interactions afforded by the 3MIC has unique
396 advantages. For example, we were excited to observe that the movement of macrophages
397 towards tumor structures, seemed to be driven by tumor cells mechanically dragging
398 macrophages into their clusters (see for example Video S7). It is possible then, that immune
399 infiltration of tumors is aided by physical recruitment by tumor cells. While we are not aware of
400 previous reports about this behavior, this may be due to the challenges of observing tumor-
401 macrophage interactions *in vivo*, especially in ischemic tumor regions.

402 It has been difficult to discern whether a decrease in drug response *in vivo* is due to lower drug
403 concentration or to intrinsic changes that make cells more drug resistant[85]. This is particularly
404 true in more fibrotic and ischemic tumors such as pancreatic ductal adenocarcinomas[86,87]. The
405 3MIC however allows for the separation of these effects and we were able to show that
406 ischemic cells display a true paclitaxel resistance mechanism. This proof-of-principle shows that
407 the 3MIC can be used to screen for genetic and pharmacological perturbations that may prevent
408 the increase of migratory behaviors triggered by ischemia while accounting for different
409 mechanisms of drug resistance.

410 Finally, the fabrication of the 3MIC is easy and affordable requiring only a conventional 3D
411 printer. This system seamlessly integrates existing co-culture and *ex vivo* protocols with only
412 small modifications. Thus, we invite the research community to use the 3MIC to study
413 metastasis and other processes where the limitation of nutrients in 3D multicellular structures is
414 relevant.

415 **METHODS**

416 **Cell culture**

417 Lung KP clones and Lung KPKeap1 clones were derived in the $KRAS^{G12D}/TP53^{-/-}$ and
418 $KRAS^{G12D}/TP53^{-/-}/Keap1^{-/-}$lung adenocarcinoma model, respectively, developed and kindly
419 shared by Dr. Thales Papagiannakopoulos. MCF10A, MCF7, DID1 cells, and SVEC-4-10 cells
420 were purchased from ATCC. C6-HRE-GFP cells were a kind gift from Dr Inna Serganova
421 (Memorial Sloan Kettering Cancer Center, New York, NY, USA). Cells were cultured in High
422 Glucose DMEM (Gibco, #11965-092) supplemented with 10% Fetal Bovine Serum (FBS;
423 Sigma-Aldrich, #F0926) at 5% CO_2 and 37°C. MCF10A cells were cultured in High Glucose
424 DMEM (Gibco, #11965-092) supplemented with 5% Horse Serum, 20ng/ml Animal-Free
425 Recombinant Human Epidermal Growth Factor (Peprotech ,#AF-100-15) , 0.5 mg/ml
426 Hydrocortisone (Sigma-Aldrich, #H0888), 100 ng/ml Cholera Toxin (Sigma-Aldrich, C8052),
427 10µg/ml Insulin, at 5% CO_2 and 37°C. Lung KP cells stably expressing a hypoxia reporter
428 (pLenti-5XHRE-GFP, Addgene #128958, denoted here as HRE-GFP), cell membrane marker
429 (pLenti-mCherry-CAAX, Addgene #129285), E-cadherin reporter (pHAGE-E-cadherin-RFP,
430 Addgene #79603), cell cycle reporter (pBOB-EF1-FastFUCCI-Puro, Addgene #86849), LV-YFP
431 (Addgene #26000), and pLenti-H2B-iRFP720 (Addgene #128961) were generated using
432 standard lentivirus mediated stable cell lone preparation protocols. H2B-mCherry was cloned by
433 removing YFP from the LV-YFP vector using BamHI and KpnI restriction enzymes. The
434 linearized vector containing H2B was then ligated with mCherry using SLIC[88].

435 **Formation of 3D tumor spheroids**

436 Cell spheroids were formed via hanging drops following standard protocols[89]. Briefly, cells were
437 dissociated into a single-cell suspension of 10^4 cells/ml. The cell suspension was distributed into
438 20μl droplets onto the lid of a Petri dish. The base of the dish was filled with PBS (Gibco,
439 #14040-133) or distilled water to prevent droplet evaporation during the incubation time. The lid
440 was then inverted onto the dish and incubated for 96 hours, to ensure the formation of compact
441 spheroids. Typically, we cultured ~50 spheroids in each 3MIC chamber.

442 **Isolation and differentiation of BMDMs**

443 Bone marrow-derived macrophages (BMDMs) were extracted from C57BL/6 mice following
444 standard protocols[45,48]. Following isolation of the bone marrow, cells were cultured in low
445 attachment culture dishes (VWR, #25384-342) in High Glucose DMEM supplemented with 10%
446 FBS and 10ng/mL Recombinant Mouse CSF-1 (R&D Systems, #416-ML) for 7 days.

447 **Establishment of tumor-derived clones**

448 Approximately $5x10^4$ cells Lung KP cells, stably expressing pLenti-5XHRE-GFP and pLenti-
449 mCherry-CAAX were injected subcutaneously into C57BL/6 mice and grown for 14 days.
450 Tumors were then extracted and dissociated using a solution containing of 2U/ml Dispase and
451 4mg/ml Collagenase IV. Cells were then sorted using FACS according GFP levels. GFP-
452 positive and negative cells were grown separately as clusters using the hanging drop method
453 described above.

454 **3D printing and microfabrication**

455 To create the framework of 3MIC fused filament fabrication was used. Designing of the
456 framework was done using openSCAD (https://openscad.org). 3MICs were printed in two parts
457 that were later assembled: the main framework and the upper coverslip holder (where consumer
458 cells are grown). These parts were printed in an Ultimaker 3B printer using Black PLA filament.
459 Alternatively, the framework can be printed using Stereolithography (SLA) printers. In this case,
460 the entire framework (the upper coverslip holder and main framework) can be printed as one
461 unit. We used Formlabs's Dental SG resin to print the framework on Form 3 (Formlabs). The
462 uncured resin was removed from the prints by washing them in isopropanol for 1 h and further
463 post-curing it with UV irradiation heated at 60°C. A glass coverslip (VWR, No. 1, 22x60mm,
464 #48393-070) was glued to the base of the main framework using a UV-curable adhesive
465 (Norland Products, NOA68) using a long-wave UV lamp (MelodySusie, DR-5401). Then, the
466 coverslip holder fragment was glued onto the glass coverslip. Finally, the assembled 3MIC was
467 sterilized in a short-wave UV lamp chamber (Meishida, CM-2009) for 15 minutes.

468 **Culture of tumor spheroids in the 3MIC**

469 To prepare the layer of consumer cells, 24hrs before the day of the experiment, a coverslip
470 (VWR, No. 2, 18x18 mm, #48366-045) was coated with Poly-D-lysine (Sigma-Aldrich, #P6407)

471 to aid adherence of cells to the glass surface. Cells were detached using trypsin and diluted into
472 a cell suspension of a density of $3.5x10^5$ cells/mL for faster dividing cells and 10^6 cells/mL for
473 slower dividing cells. The coverslip was placed into a well of a 6-well dish and covered with 1mL
474 of the cell suspension. The coverslip was incubated overnight at 37°C to let the cells adhere to
475 the coverslip. On the day of the experiment, the spheroids were collected from the Petri dishes
476 by inverting the lid and gently flushing all the spheroids with DMEM supplemented with 10%
477 FBS using a 5mL serological pipette. The spheroid containing suspension was collected and
478 centrifuged at 50G for 10-15 minutes. Meanwhile, a thin bed of 110μL ECM was made in the
479 3MIC – here, we used either 2.2mg/mL rat tail Collagen (Corning, #354236) – or 2:3 mix of
480 Matrigel and 1.6mg/ml of rat tail Collagen I and incubated at 37°C for 20 mins to allow the
481 polymerization of the ECM. Spheroids were resuspended in about 110μL of ECM and
482 immediately transferred onto the polymerized ECM bed. The ECM with spheroids was
483 polymerized at 37°C for ~30 minutes. With the help of forceps, the coverslip containing the
484 consumer cells was inverted and inserted into the slot of the coverslip holder. The 3MIC was
485 then gently filled with 1.25mL of media, avoiding trapping bubbles underneath the consumer
486 coverslip. Control wells are assembled in the same way, but the top coverslip has no consumer
487 cells.

488 **Collagen degradation assay**

489 To investigate the invasive potential of cells across the gradient, the ECM was mixed with DQ-
490 collagen, type I From Bovine Skin, Fluorescein Conjugate (Invitrogen, #D12060) at a final
491 concentration of 25μg/ml. This ECM was used to prepare the bed and embed the spheroids as
492 well. The extent of degradation of the matrix was determined by measuring the fluorescence
493 intensity of cleaved collagen.

494 **Gelatin degradation assay**

495 Glass coverslips were coated with gelatin from pig skin, Oregon Green 488 Conjugate (Thermo
496 Fisher Scientific, #G13186), by inverting coverslips on 20µl drops of fluorescent gelatin
497 (1mg/ml) and incubating for 20 minutes. The coverslips were then lifted, excess liquid drained,
498 and inverted on 40µl drops of 0.5% glutaraldehyde for fixation. The coverslips were then
499 washed with PBS and glued onto the PLA frame using the UV-curable adhesive (Norland

500 Products, #NOA68) and cured in a long-wave UV lamp (MelodySusie, #DR-5401) for 15
501 minutes. The cured coverslip was then UV-sterilized and used for the experiment. Briefly, the
502 spheroids were collected from the hanging drops and centrifuged and resuspended in 100µl of
503 media. The spheroid solution was carefully placed on the coated coverslips and incubated for
504 30-60 minutes to allow the spheroids to settle down. After ensuring that there are no floating
505 spheroids, the consumer coverslip was transferred into the 3MIC and the remaining 1.4ml of
506 media was added. The 3MICs were incubated at 37°C, for 24 hours. After 24 hours, the 3MICs
507 were fixed using 4% paraformaldehyde (PFA) for 10 mins and imaged using 10X objective of
508 Nikon Eclipse Ti2-E spinning disk confocal microscope.

509 **Microscopy**

510 Microscopic images were captured using a 10x objective of Nikon Eclipse Ti2-E spinning disk
511 confocal microscope, at fixed timepoints or set up for time-lapse microscopy. For time-lapse
512 microscopy, cells were maintained at 37°C using a stage top incubator (Tokai Hit, #INUCG2-
513 KRi) and the chamber was connected to a humidified mixed gas source (5% CO_2). Spheroids
514 from different regions of the 3MIC were imaged at suitable time-intervals in different fluorescent
515 channels. Typically, we imaged ~10 spheroids per 3MIC every 15-30 mins for 24h.

516 **Immunofluorescence**

517 Spheroids within the 3MIC were fixed using 4% PFA (Affymetrix, #19943) for 10 minutes at
518 room temperature and washed four times with PBS. Cultures were permeabilized using PBS
519 containing 0.5% (vol/vol) Triton-X-100 (Sigma-Aldrich, #T8787) for 20 minutes and washed
520 three times with PBS. Slides were blocked in 10% FBS in immunofluorescence (IF) buffer (0.3M
521 glycine in PBS) for 60 minutes at room temperature. Primary antibodies were diluted at 1:200 in
522 the same blocking solution. We used anti-phospho-H3 (Cell Signaling Technologies, #9706), E-
523 cadherin (BD Bio Sciences, #610182), and CD45 (R&D, #AF114) antibodies. 3MICs were
524 incubated with primary antibodies overnight at 4°C, then washed with IF buffer and incubated
525 overnight at 4°C with secondary antibodies also diluted in blocking solution at 1:200. Cultures
526 were then washed and counterstained with 0.5µg/mL Hoechst 33342 in PBS (Invitrogen,
527 #H1399).

528 **Image analysis**

529 Automated cell tracking was conducted as previously described[48]. Persistence is defined as the
530 ratio between the net displacement of a cell over its trajectory. We estimated the local cell
531 density using a method based on the Delaunay triangulation of neighboring cells[45,48]. Per cell,
532 per spheroid, and population levels of florescence were estimated using custom image analysis
533 software as previously described[44].

534 **Cellular Potts Model (CPM) simulations**

535 Simulations were conducted using a MATLAB CPM implementation[90]. Adhesion between core
536 (C1) and cortical (C2) cells were implemented as:

537 $$J_{C1,C1} > J_{C1,C2} > J_{C2,C2}$$

538 Where $J_{i,j}$ is the surface energy at every contact point between the two cells[62]. This relationship
539 modeled the decrease in E-Cad levels in ischemic cells. The differential affinity for the ECM in
540 core cells was simulates as:

541 $$J_{C1,ECM} < J_{C2,ECM}$$

542 The CPM was implemented in a 200x200 grid with 100 initial cells and run for $1{,}28 \times 10^8$ Monte
543 Carlo Simulation steps. Parameters used in the conditions presented here can be found in
544 Tables S1 and S2. MATLAB routines to run the simulations are available upon request.

545 **Statistics**

546 We conducted at least three biological replicates of all experiments. Unless noted, we used two-
547 tailed t-student tests to estimate p-values between two conditions and Pearson's linear
548 coefficient when testing correlations. For multiple comparisons, we used one-way ANOVA
549 followed by a Tukey-Kramer test. In all plots, error bars show standard deviation from the mean.
550 In boxplots, center lines show the median and box edges show 75th and 25th empirical quartiles
551 of the data.

552 **ACKNOWLEDGEMENTS**

We thank all members of the Carmofon Laboratory for critical discussions about this project and the manuscript. This work was supported by awards to CC-F from the National Cancer Institute of NIH (DP2 CA250005) and the American Cancer Society (RSG-21-179-01-TBE). CC-F is a Pew Scholar in the Biomedical Sciences, supported by The Pew Charitable Trust (00034121). JG was partially funded by a NIH Training Grant (1T32GM132037-01).

Authors contributions: Concept and experimental design CC-F with help from LA. Experiments by LA, JG, JL, MR, and C-CF. Image analysis: CC-F, LA, and LJ. Mathematical modeling: CC-F. Manuscript written by CC-F with feedback and contributions from all authors.

Competing interests: NYU is pursuing a patent for the 3MIC and related systems where CC-F is listed as inventor.

Data and materials availability: All data is available in the manuscript or the supplementary materials. Original raw files and analysis software are available upon request. Use of the 3MIC requires a Material Transfer Agreement and it is free for non-commercial and academic uses.

ADDITIONAL INFORMATION

Supplementary information is available for this paper. Correspondence and requests for materials should be addressed to CC-F.

1. Lambert, A. W., Pattabiraman, D. R. & Weinberg, R. A. Emerging Biological Principles of Metastasis. *Cell* **168**, 670–691 (2017).

2. Welch, D. R. & Hurst, D. R. Defining the Hallmarks of Metastasis. *Cancer Res* **79**, 3011–3027 (2019).

3. Chaffer, C. L. & Weinberg, R. A. A perspective on cancer cell metastasis. *Science (1979)* **331**, 1559–1564 (2011).

4. Siegel, R. L., Miller, K. D., Fuchs, H. E. & Jemal, A. Cancer statistics, 2022. *CA Cancer J Clin* **72**, 7–33 (2022).

5. Tasdogan, A., Ubellacker, J. M. & Morrison, S. J. Redox regulation in cancer cells during metastasis. *Cancer Discov* **11**, 2682–2692 (2021).

6. García-Jiménez, C. & Goding, C. R. Starvation and Pseudo-Starvation as Drivers of Cancer Metastasis through Translation Reprogramming. *Cell Metab* **29**, 254–267 (2019).

7. Rankin, E. B. & Giaccia, A. J. Hypoxic control of metastasis. *Science* **352**, 175–80 (2016).

8. Fais, S., Venturi, G. & Gatenby, B. Microenvironmental acidosis in carcinogenesis and metastases: new strategies in prevention and therapy. *Cancer and Metastasis Reviews* **33**, 1095–1108 (2014).

9. Quail, D. F. & Joyce, J. A. Microenvironmental regulation of tumor progression and metastasis. *Nat Med* **19**, 1423–1437 (2013).

10. Massagué, J. & Ganesh, K. Metastasis-Initiating Cells and Ecosystems. *Cancer Discov* **11**, 971–994 (2021).

11. Condeelis, J. & Pollard, J. W. Macrophages: Obligate Partners for Tumor Cell Migration, Invasion, and Metastasis. *Cell* **124**, 263–266 (2006).

12. Ganesh, K. & Massagué, J. Targeting metastatic cancer. *Nature Medicine 2021 27:1* **27**, 34–44 (2021).

13. Iacobuzio-Donahue, C. A. *et al.* Cancer biology as revealed by the research autopsy. *Nature Reviews Cancer 2019 19:12* **19**, 686–697 (2019).

14. Ring, A., Nguyen-Sträuli, B. D., Wicki, A. & Aceto, N. Biology, vulnerabilities and clinical applications of circulating tumour cells. *Nat Rev Cancer* (2022) doi:10.1038/S41568-022-00536-4.

15. Hosseini, H. *et al.* Early dissemination seeds metastasis in breast cancer. *Nature 2016 540:7634* **540**, 552–558 (2016).

16. Klein, C. A. Parallel progression of primary tumours and metastases. *Nature Reviews Cancer 2009 9:4* **9**, 302–312 (2009).

17. Makohon-Moore, A. P. *et al.* Precancerous neoplastic cells can move through the pancreatic ductal system. *Nature 2018 561:7722* **561**, 201–205 (2018).

18. Chen, L. L., Blumm, N., Christakis, N. A., Barabási, A. L. & Deisboeck, T. S. Cancer metastasis networks and the prediction of progression patterns. *British Journal of Cancer 2009 101:5* **101**, 749–758 (2009).

19. Harper, K. L. *et al.* Mechanism of early dissemination and metastasis in Her2+ mammary cancer. *Nature 2016 540:7634* **540**, 588–592 (2016).

20. Khanna, C. & Hunter, K. Modeling metastasis in vivo. *Carcinogenesis* **26**, 513–523 (2005).

21. Fontebasso, Y. & Dubinett, S. M. Drug Development for Metastasis Prevention. *Crit Rev Oncog* **20**, 449–474 (2015).

22. Anderson, R. L. *et al.* A framework for the development of effective anti-metastatic agents. *Nature Reviews Clinical Oncology 2018 16:3* **16**, 185–204 (2018).

23. Gould, S. E., Junttila, M. R. & de Sauvage, F. J. Translational value of mouse models in oncology drug development. *Nature Medicine 2015 21:5* **21**, 431–439 (2015).

24. Day, C. P., Merlino, G. & Van Dyke, T. Preclinical Mouse Cancer Models: A Maze of Opportunities and Challenges. *Cell* **163**, 39–53 (2015).

25. Gilkes, D. M., Semenza, G. L. & Wirtz, D. Hypoxia and the extracellular matrix: drivers of tumour metastasis. (2014) doi:10.1038/nrc3726.

26. Nobre, A. R., Entenberg, D., Wang, Y., Condeelis, J. & Aguirre-Ghiso, J. A. The Different Routes to Metastasis via Hypoxia-Regulated Programs. *Trends Cell Biol* **28**, 941–956 (2018).

27. Bergers, G. & Fendt, S. M. The metabolism of cancer cells during metastasis. *Nature Reviews Cancer 2021 21:3* **21**, 162–180 (2021).

28. Lehúede, C., Dupuy, F., Rabinovitch, R., Jones, R. G. & Siegel, P. M. Metabolic plasticity as a determinant of tumor growth and metastasis. *Cancer Res* **76**, 5201–5208 (2016).

29. Bergers, G. & Benjamin, L. E. Tumorigenesis and the angiogenic switch. *Nat Rev Cancer* **3**, 401–410 (2003).

30. Gatenby, R. A. & Gillies, R. J. A microenvironmental model of carcinogenesis. *Nat Rev Cancer* **8**, 56–61 (2008).

31. Lyssiotis, C. A. & Kimmelman, A. C. Metabolic Interactions in the Tumor Microenvironment. *Trends Cell Biol* **27**, 863–875 (2017).

32. Hobson-Gutierrez, S. A. & Carmona-Fontaine, C. The metabolic axis of macrophage and immune cell polarization. *Dis Model Mech* **11**, dmm034462 (2018).

33. Bader, J. E., Voss, K. & Rathmell, J. C. Targeting Metabolism to Improve the Tumor Microenvironment for Cancer Immunotherapy. *Mol Cell* **78**, 1019–1033 (2020).

34. Gatenby, R. A. & Gillies, R. J. Why do cancers have high aerobic glycolysis? *Nat Rev Cancer* **4**, 891–899 (2004).

35. Thomlinson, R. H. Hypoxia and tumours. *Journal of clinical pathology PMID - 269113* **11**, 105–113 (1977).

36. Vaupel, P., Kallinowski, F. & Okunieff, P. Blood flow, oxygen and nutrient supply, and metabolic microenvironment of human tumors: a review. *Cancer Res* **49**, 6449–65 (1989).

37. Gillies, R. J. & Gatenby, R. A. Hypoxia and adaptive landscapes in the evolution of carcinogenesis. *Cancer and Metastasis Reviews* **26**, 311–317 (2007).

38. Robey, I. F. *et al.* Bicarbonate increases tumor pH and inhibits spontaneous metastases. *Cancer Res* **69**, 2260–2268 (2009).

39. Borriello, L. *et al.* Primary tumor associated macrophages activate programs of invasion and dormancy in disseminating tumor cells. *Nature Communications 2022 13:1* **13**, 1–19 (2022).

40. Boj, S. F. *et al.* Organoid Models of Human and Mouse Ductal Pancreatic Cancer. *Cell* **160**, 324–338 (2015).

41. Gao, D. *et al.* Organoid Cultures Derived from Patients with Advanced Prostate Cancer. *Cell* **159**, 176–187 (2014).

42. Neal, J. T. *et al.* Organoid Modeling of the Tumor Immune Microenvironment. *Cell* **175**, 1972-1988.e16 (2018).

43. Tuveson, D. & Clevers, H. Cancer modeling meets human organoid technology. *Science* **364**, 952–955 (2019).

44. Janská, L. *et al.* The MEMIC is an ex vivo system to model the complexity of the tumor microenvironment. *DMM Disease Models and Mechanisms* **14**, (2021).

45. Carmona-Fontaine, C. *et al.* Metabolic origins of spatial organization in the tumor microenvironment. *Proceedings of the National Academy of Sciences* **114**, 2934–2939 (2017).

46. Sánchez-Rivera, F. J. *et al.* Rapid modelling of cooperating genetic events in cancer through somatic genome editing. *Nature* **516**, 428–431 (2014).

47. Serganova, I. *et al.* Metabolic imaging: A link between lactate dehydrogenase A, lactate, and tumor phenotype. *Clinical Cancer Research* **17**, (2011).

48. Carmona-Fontaine, C. *et al.* Emergence of spatial structure in the tumor microenvironment due to the Warburg effect. *Proceedings of the National Academy of Sciences* **110**, 19402–19407 (2013).

49. Wu, P. H., Giri, A., Sun, S. X. & Wirtz, D. Three-dimensional cell migration does not follow a random walk. *Proc Natl Acad Sci U S A* **111**, 3949–3954 (2014).

50. Mardia, K. V. & Jupp, P. E. *Directional statistics*. (J. Wiley, 2000).

51. Moon, E. J. *et al.* The HIF target MAFF promotes tumor invasion and metastasis through IL11 and STAT3 signaling. *Nature Communications 2021 12:1* **12**, 1–18 (2021).

52. Polyak, K. & Weinberg, R. A. Transitions between epithelial and mesenchymal states: acquisition of malignant and stem cell traits. *Nature Reviews Cancer 2009 9:4* **9**, 265–273 (2009).

53. Scheel, C., Onder, T., Karnoub, A., Weinberg, R. A. & Talmadge, J. E. Adaptation versus Selection: The Origins of Metastatic Behavior. *Cancer Res* **67**, 11476–11480 (2007).

54. Padmanaban, V. *et al.* E-cadherin is required for metastasis in multiple models of breast cancer. *Nature* **573**, 439–444 (2019).

55. Chen, J., Imanaka, N., Chen, J. & Griffin, J. D. Hypoxia potentiates Notch signaling in breast cancer leading to decreased E-cadherin expression and increased cell migration and invasion. *British Journal of Cancer 2010 102:2* **102**, 351–360 (2009).

56. Dongre, A. & Weinberg, R. A. New insights into the mechanisms of epithelial–mesenchymal transition and implications for cancer. *Nat Rev Mol Cell Biol* **20**, 69–84 (2018).

57. Lehmann, S. *et al.* Hypoxia Induces a HIF-1-Dependent Transition from Collective-to-Amoeboid Dissemination in Epithelial Cancer Cells. *Current Biology* **27**, 392–400 (2017).

58. Jiang, L. *et al.* Metabolic reprogramming during TGFβ1-induced epithelial-to-mesenchymal transition. *Oncogene 2015 34:30* **34**, 3908–3916 (2014).

59. Ros, M. *et al.* ER-resident oxidoreductases are glycosylated and trafficked to the cell surface to promote matrix degradation by tumour cells. *Nature Cell Biology 2020 22:11* **22**, 1371–1381 (2020).

60. Sloane, B. F., Sameni, M., Podgorski, I., Cavallo-Medved, D. & Moin, K. Functional Imaging of Tumor Proteolysis. *Annu Rev Pharmacol Toxicol* **46**, 301–315 (2006).

61. Glazier, J. A. & Graner, F. Simulation of the differential adhesion driven rearrangement of biological cells. *Phys Rev E* **47**, 2128 (1993).

62. Graner, F. & Glazier, J. A. Simulation of biological cell sorting using a two-dimensional extended Potts model. *Phys Rev Lett* **69**, 2013 (1992).

63. Szabó, A. & Merks, R. M. H. Cellular Potts modeling of tumor growth, tumor invasion, and tumor evolution. *Front Oncol* **3 APR**, 87 (2013).

64. Godet, I. *et al.* Fate-mapping post-hypoxic tumor cells reveals a ROS-resistant phenotype that promotes metastasis. *Nat Commun* **10**, 4862 (2019).

65. Labuschagne, C. F., Cheung, E. C., Blagih, J., Domart, M. C. & Vousden, K. H. Cell Clustering Promotes a Metabolic Switch that Supports Metastatic Colonization. *Cell Metab* **30**, 720-734.e5 (2019).

66. Wenes, M. *et al.* Macrophage Metabolism Controls Tumor Blood Vessel Morphogenesis and Metastasis. *Cell Metab* **24**, 701–715 (2016).

67. Linde, N. *et al.* Macrophages orchestrate breast cancer early dissemination and metastasis. *Nat Commun* **9**, 21 (2018).

68. Gocheva, V. *et al.* IL-4 induces cathepsin protease activity in tumor-associated macrophages to promote cancer growth and invasion. *Genes Dev* **24**, 241–255 (2010).

69. Colegio, O. R. *et al.* Functional polarization of tumour-associated macrophages by tumour-derived lactic acid. *Nature* **513**, 559–563 (2014).

70. Noy, R. & Pollard, J. W. Tumor-Associated Macrophages: From Mechanisms to Therapy. *Immunity* **41**, 49–61 (2014).

71. Bronte, V. & Murray, P. J. Understanding local macrophage phenotypes in disease: modulating macrophage function to treat cancer. *Nat Med* **21**, 117–119 (2015).

72. Weaver, B. A. How Taxol/paclitaxel kills cancer cells. *Mol Biol Cell* **25**, 2677–2681 (2014).

73. Belotti, D. *et al.* Paclitaxel (Taxol#{174}) Inhibits Motility of Paclitaxel-resistant Human Ovarian Carcinoma Cells'. **2**, 1725–1730 (1996).

74. Wang, X., Decker, C. C., Zechner, L., Krstin, S. & Wink, M. In vitro wound healing of tumor cells: Inhibition of cell migration by selected cytotoxic alkaloids. *BMC Pharmacol Toxicol* **20**, 1–12 (2019).

75. Gould, S. E., Junttila, M. R. & Sauvage, F. J. de. Translational value of mouse models in oncology drug development. *Nat Med* **21**, 431–9 (2015).

76. Hobson-Gutierrez, S. A. & Carmona-Fontaine, C. The metabolic axis of macrophage and immune cell polarization. *DMM Disease Models and Mechanisms* **11**, (2018).

77. Püschel, F. *et al.* Starvation and antimetabolic therapy promote cytokine release and recruitment of immune cells. *Proc Natl Acad Sci U S A* **117**, 9932–9941 (2020).

78. Lee, J. G. *et al.* Intronic regulation of matrix metalloproteinase-2 revealed by in vivo transcriptional analysis in ischemia. *Proc Natl Acad Sci U S A* **102**, 16345–16350 (2005).

79. Chaturvedi, M. & Kaczmarek, L. MMP-9 Inhibition: a Therapeutic Strategy in Ischemic Stroke. *Molecular Neurobiology 2013 49:1* **49**, 563–573 (2013).

80. Chen, J., Imanaka, N., Chen, J. & Griffin, J. D. Hypoxia potentiates Notch signaling in breast cancer leading to decreased E-cadherin expression and increased cell migration and invasion. *Br J Cancer* **102**, 351–60 (2009).

81. Fischer, K. R. *et al.* Epithelial-to-mesenchymal transition is not required for lung metastasis but contributes to chemoresistance. *Nature* **527**, 472–6 (2015).

82. Wadhams, G. H. & Armitage, J. P. Making sense of it all: bacterial chemotaxis. *Nature Reviews Molecular Cell Biology 2004 5:12* **5**, 1024–1037 (2004).

83. Gerisch, G. Chemotaxis in Dictyostelium. *https://doi.org/10.1146/annurev.ph.44.030182.002535* **Vol. 44**, 535–552 (2003).

84. Labuschagne, C. F., Cheung, E. C., Blagih, J., Domart, M.-C. & Vousden, K. H. Cell Clustering Promotes a Metabolic Switch that Supports Metastatic Colonization. *Cell Metab* **30**, 720-734.e5 (2019).

85. Dewhirst, M. W. & Secomb, T. W. Transport of drugs from blood vessels to tumour tissue. *Nature Reviews Cancer 2017 17:12* **17**, 738–750 (2017).

86. Teicher, B. A. Hypoxia and drug resistance. *Cancer and Metastasis Reviews* **13**, 139–168 (1994).

87. Rohwer, N. & Cramer, T. Hypoxia-mediated drug resistance: Novel insights on the functional interaction of HIFs and cell death pathways. *Drug Resistance Updates* **14**, 191–201 (2011).

88. Jeong, J. Y. *et al.* One-step sequence-and ligation-independent cloning as a rapid and versatile cloning method for functional genomics Studies. *Appl Environ Microbiol* **78**, 5440–5443 (2012).

89. Vinci, M., Box, C., Zimmermann, M. & Eccles, S. A. Tumor spheroid-based migration assays for evaluation of therapeutic agents. *Methods in Molecular Biology* **986**, 253–266 (2013).

90. Tsuyoshi Hirashima. Primer for cellular Potts model. *https://www.mathworks.com/matlabcentral/fileexchange/64207-primer-for-cellular-potts-model*.

FIGURES

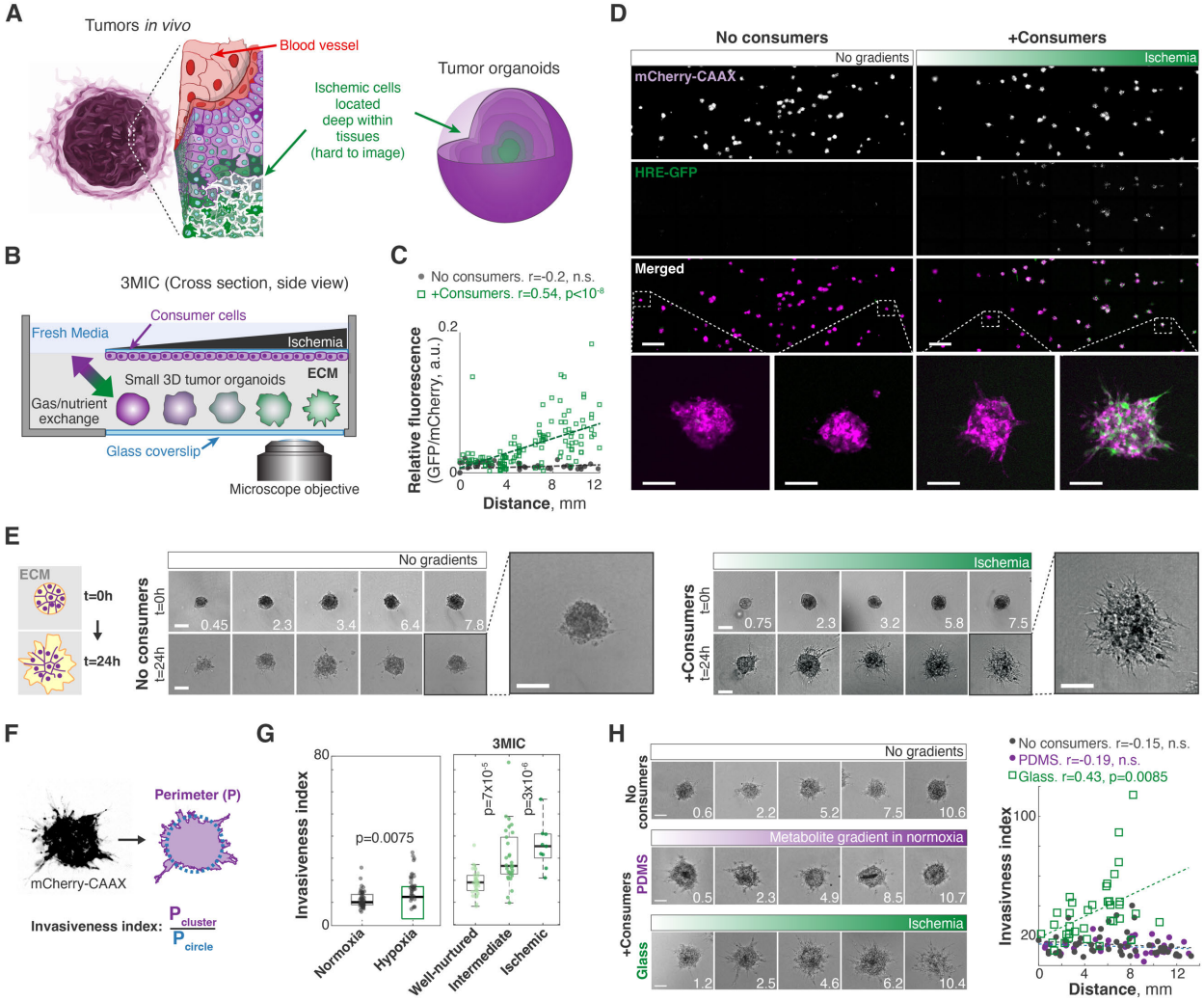

Figure 1: Design and implementation of a metabolic microenvironment chamber for 3D cultures

A. Cartoons showing ischemic regions in solid tumor and conventional tumor organoids. Cells in these regions are hard to access and to image.

B. Schematic cross-section of the 3MIC where a monolayer of "consumer" cells grows on the top of a small chamber. Tumor spheroids grow embedded in ECM within the same chamber and underneath consumer cells. This small chamber is connected to a large reservoir of fresh media from only on one side (left) where nutrient and gas exchanges occur.

C. Quantification of *per* spheroid GFP levels from HRE-GFP Lung KP 3D spheroids cultured in the 3MIC (~100cells/spheroid). GFP levels serve as a proxy for hypoxia and are normalized to constitutive mCherry-CAAX signal. Dashed line: linear fit.

D. Low magnification showing GFP and mCherry fluorescence in tumor spheroids cultured alone (left column) or in the presence of consumer cells (right column) along the 3MIC gradient. Bottom panels zoom into representative individual tumor spheroids. Bars: 1000μm, 100μm for insets.

E. Left: Lung KP spheroids imaged after 0h (top) and 24h (bottom) of growth in different regions of the 3MIC without consumer cells. These clusters grew uniformly and retained smooth and round shapes.

Right: Similar data but for spheroids grown in the presence of consumer cells. Ischemic spheroids grew larger and more protrusive. Numbers in lower right corner denote the distance to the opening in mm. Bars: 100μm.

F. We defined invasiveness index, as the perimeter of tumor spheroid over the perimeter of a circle with the same area (1/circularity).

G. Using the invasiveness index, we quantified the invasiveness of lung KP cluster under different environments. Well-nurtured, intermediate, and ischemic condition correspond to different regions of the 3MIC. Data points: *per* spheroid invasiveness.

H. Representative images of individual spheroids grown for 24h in the absence of consumer cells (top), or in the presence of consumer cells in 3MICs enclosed in PDMS (Polydimethylsiloxane) or glass (center and bottom). Numbers in lower right corner denote the distance to the chamber's opening in mm. Bars: 100μm. Plots on the right show a quantification of these changes. Data points: invasiveness index of individual spheroids. Dash lines: linear fit.

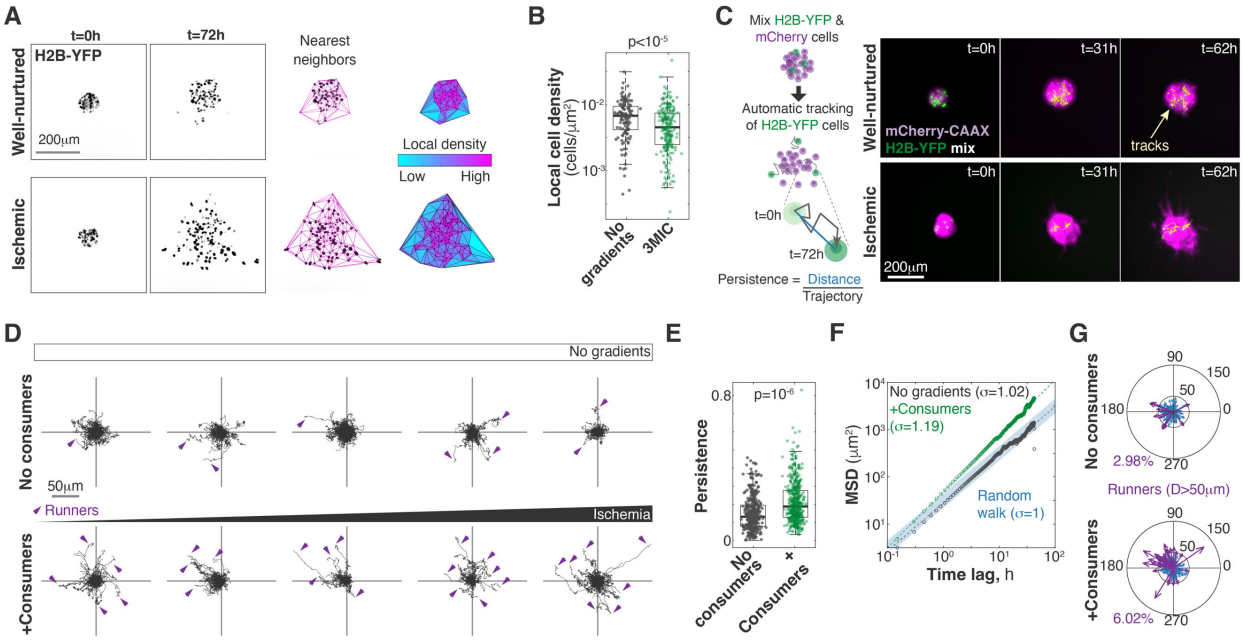

Figure 2: Ischemic cells in the 3MIC migrate more persistently

A. Image-based method to estimate local cell density. We located individual cells expressing the fluorescent nuclear marker H2B-YFP. We then triangulated closest neighbors and estimated areas between them. Local cell density is roughly the inverse of triangle areas.

B. Quantification of local cell densities over time for spheroids in the presence of absence of consumer cells.

C. Experimental setup and representative data of automatically tracked individual cells.

D. Top: Migratory tracks of cells from 5 different tumor spheroids located at increasing distances from the 3MIC's opening in the absence of consumer cells. Bottom: migratory tracks of cells from 5 different clusters located at similar distances from the opening as plots above but in the presence of consumer cells. Arrowheads show tracks of runner (defined as having a net displacement of 50μm or more).

E. Persistence of individual cells. Cells in ischemic spheroids are significantly more persistent than cells in well-nurtured spheroids.

F. Mean-squared displacement (MSD) analysis of all tracked cells. Ischemic cells disperse more than what would be expected from a random walk (MSD constant α>1).

G. Compass plots showing the direction and magnitude of final displacement for individual cells. Runner cells are highlighted in purple. 3MIC opening (higher nutrients/oxygen levels) is to the left.

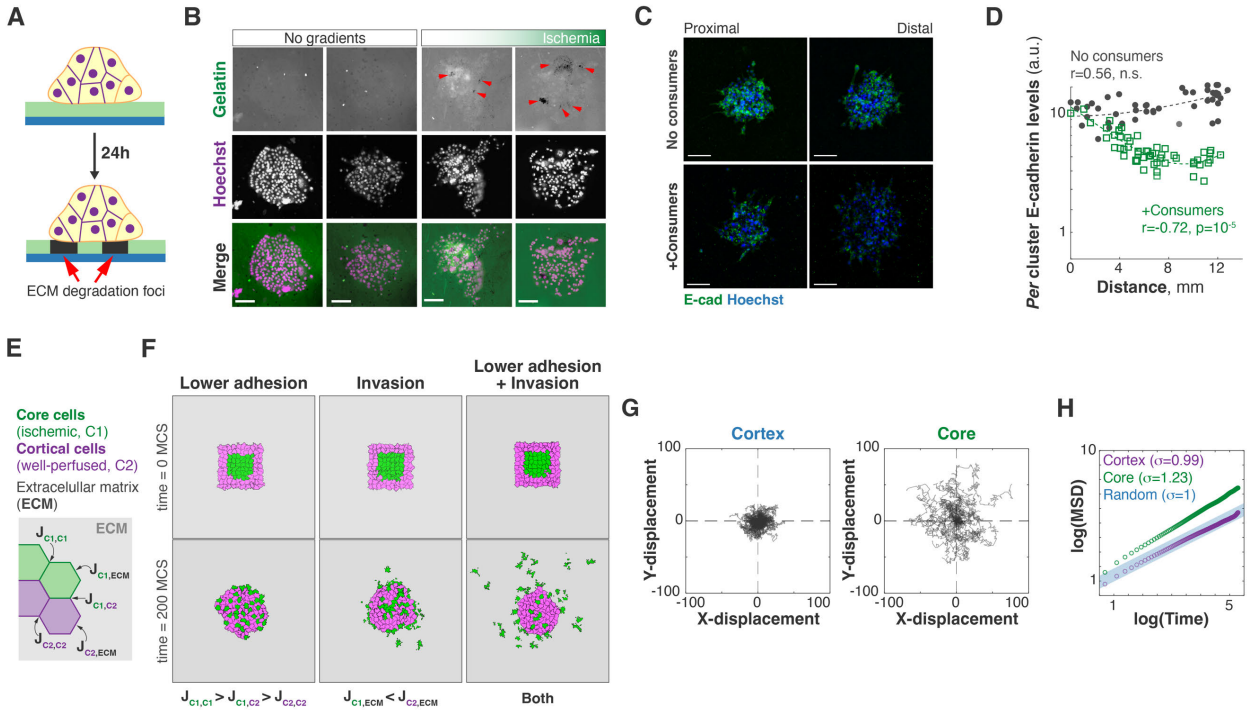

Figure 3: A decrease in epithelial adhesion and increased invasion can synergize to efficiently disperse tumor cells.

A. Schematic depicting the ECM degradation assay where spheroids are grown on a glass coated with fluorescent gelatin. Local loss of fluorescence indicates ECM degradation foci.

B. Representative images of spheroids grown in the presence or absence of consumer cells. Ischemic spheroids show higher gelatin degradation (dark spots, red arrowheads). Bars: 100μm.

C. Representative images of Lung KP spheroids grown in the 3MIC and immunostained for E-cad (green). Nuclei stained with Hoechst (blue). Bars: 100μm.

D. Quantification of E-cad levels in clusters at different locations along 3MICs with or without consumer cells. Data points: *per* spheroid E-Cad levels. Dashed line: linear fit. Bars: 100 μm.

E. Schematic depicting cell-cell and cell-substrate energies included in our Cellular Potts Model. See more details in main text and supplementary information.

F. Initial and final conditions of simulated tumor populations moving under different rules. The combination of lower epithelial adhesion and invasion, but not each process alone, efficiently increase the dispersion of ischemic (core) cells.

G. Tracks of simulated ischemic (core) and well-nurtured (cortical) cells modeled to have lower epithelial adhesion and increased invasion.

H. MSD of simulated well-nurtured and ischemic cells with lower epithelial adhesion and invasion. MSD changes are in the same order of magnitude as in our experimental data (Fig. 2F).

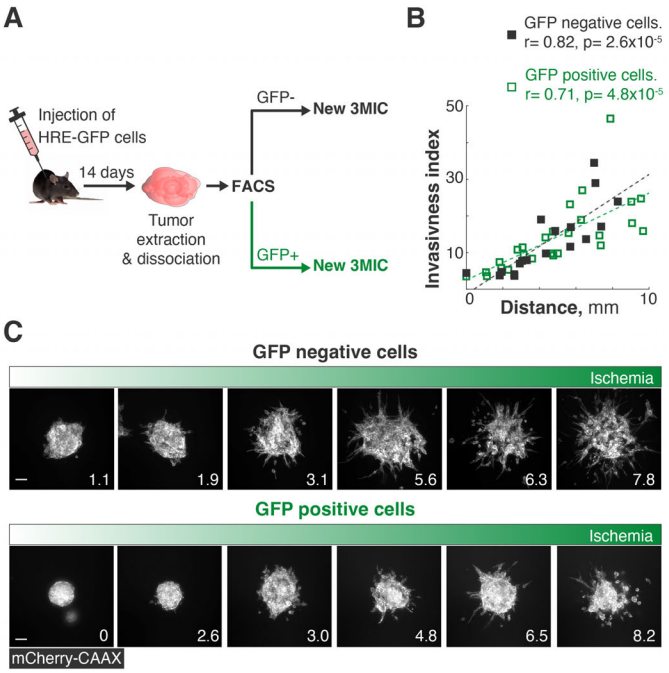

Figure 4: Tumor hypoxia *in vivo* did not induce permanent changes in the migratory potential of tumor cells.

A. Lung KP cells expressing HRE-GFP and mCherry-CAAX were injected subcutaneously in C57BL/6 mice and allowed to grow for 14 days. Tumors were then extracted and sorted into GFP positive (hypoxic/ischemic) and GFP negative (normoxic/well-nurtured) populations. These different sub-populations were grown as tumor spheroids in 3MICs in the absence or presence of consumer cells.
B. Quantification of invasiveness of experimental setup shown in (**A**). Data points: invasiveness index of individual spheroids. Dashed lines: linear fit. We observed similar invasion levels and response to ischemia in all spheroids regardless if they were derived from well-nurtured or ischemic tumor regions.
C. Representative images of tumor spheroids derived from GFP positive and GFP negative cells growing at different locations inside of 3MICs. Numbers in lower right corner denote the distance to the opening in mm. Bars: 100μm.

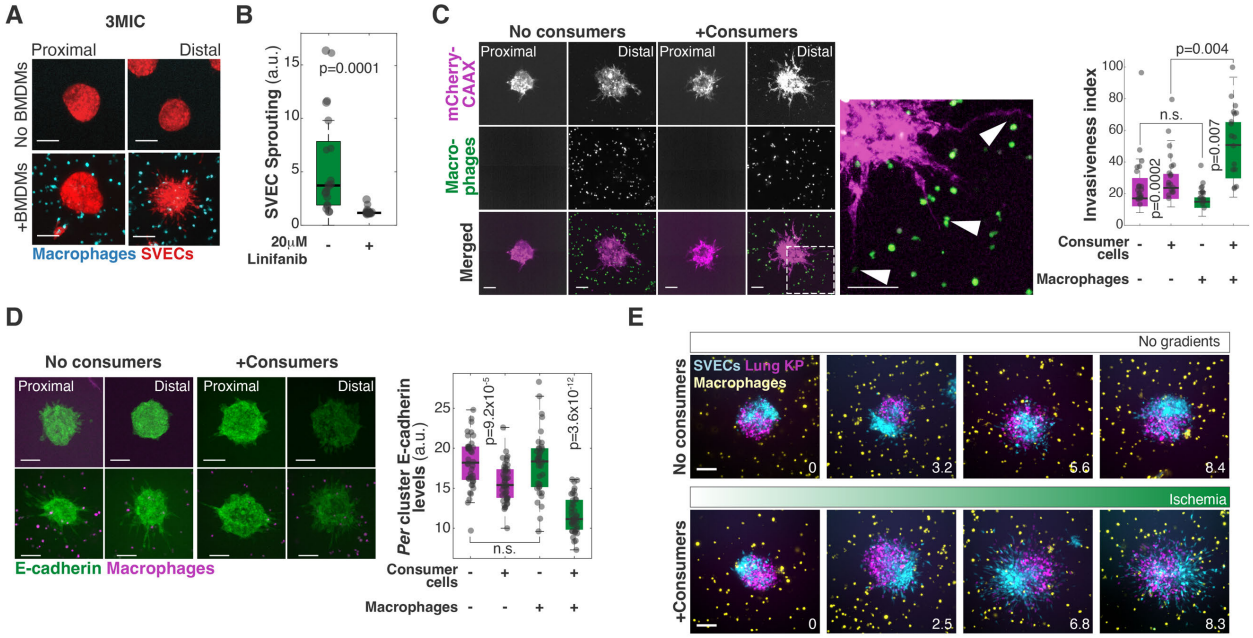

Figure 5: The 3MIC allowed the seamless implementation of cell co-cultures

A. Clusters of endothelial cells (SVECs, red) grown in 3MICs in the presence or absence of bone marrow-derived macrophages (BMDMs, cyan). Bars: 100μm.

B. Quantification of SVEC sprouting in clusters co-cultured with BMDMs. VEGFA inhibitor Linifanib abrogates sprouting induced by ischemic BMDMs.

C. Representative images and quantification of invasiveness of Lung KP spheroids co-cultured with BMDMs in the 3MIC. Ischemic macrophages significantly enhance tumor invasiveness and synergizes with ischemia. Region of delineated with dashed lines is magnified on the right. Data points: *Per* spheroid invasiveness. Bars: 100μm.

D. Representative images of lung KP spheroids grown in the 3MIC and immunostained for E-cad (green) and in the presence or absence of macrophages (magenta). Ischemia and the presence of macrophages synergize in their reduction of E-Cad levels. Bars: 100 μm.

E. Representative images of triple co-cultures: Chimeric Lung KP cells and SVEC spheroids, were grown in the presence of BMDMs with or without consumer cells. Numbers in lower right corner denote the distance to the opening in mm. Bars: 100μm.

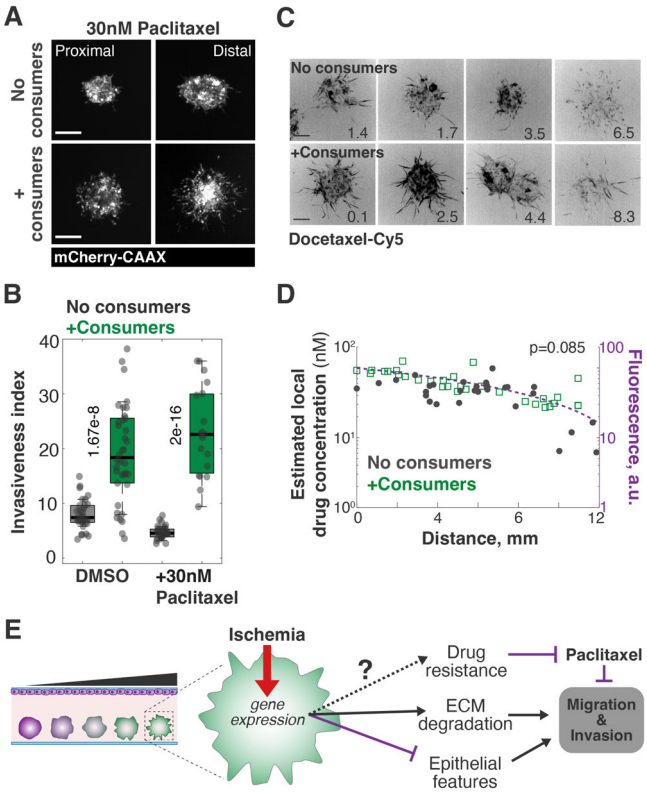

Figure 6: Ischemia induces chemoresistance in ischemic spheroids.
A. Representative images of Lung KP spheroids grown in 3MICs and treated with 30nM Paclitaxel in the presence or absence of consumer cells. Ischemic spheroids retained migratory capacity seemingly not responding to this drug. Bars: 100μm.
B. Quantification of (**A**). Points: invasiveness of individual clusters.
C. Representative images of Lung KP clusters grown in the 3MIC in the presence or absence of gradients and treated with a fluorescent paclitaxel analog (Docetaxel-Cy5). We used its fluorescent signal to estimate local levels of the drug in the 3MIC. Numbers in lower right corner denote the distance to the opening in mm. Bars: 100μm.
D. Estimated levels of paclitaxel in the presence or absence of consumer cells. Diffusion decreased drug levels in both conditions in the same magnitude. However only spheroids growing in the presence of consumer cells showed resistance to paclitaxel ruling out diffusion as the cause.
E. Summary of the data shown in this work. Ischemia enhances ECM degradation and increases tumor cell migration. These environmental conditions also lead to paclitaxel resistance.

Supplementary Information

TABLE OF CONTENTS

Supplementary Figures 2
Supplementary Video Legends 10
Supplementary Tables 14

SUPPLEMENTARY FIGURES

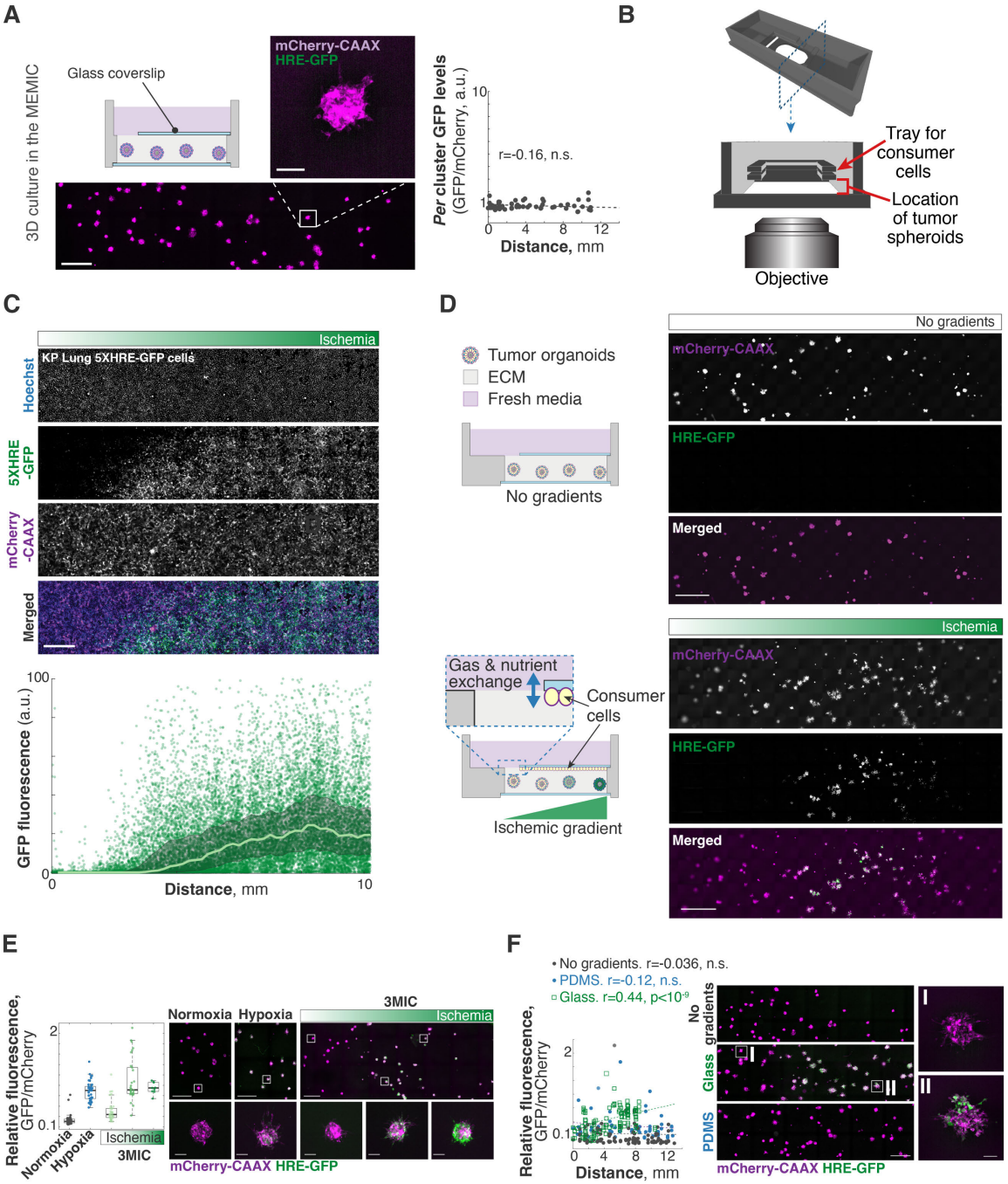

Supplementary Figure 1. Consumer cells are essential to establish a hypoxic gradient for 3MIC.
A. Spheroids grown in MEMICs fail to establish metabolic hypoxic gradients. Plot show the quantification of *per* spheroid GFP fluorescence (hypoxia reporter). Bars: 1000μm, and 100μm for insets.
B. Schematic showing the design of the 3MIC. A coverslip with attached consumer cells is slid into the holder above embedded clusters to create a nearly enclosed chamber. The rest of the structure contains fresh media.

C. Representative images of consumer cells expressing 5xHRE-GFP and mCherry-CAAX. Plot show the quantification of *per* spheroid GFP fluorescence (hypoxia reporter). Line: moving average. Bars: 100μm
D. Spheroids of C6 glioma cells stably expressing a different hypoxia reporter (hGFP[47]). Bars: 1000μm.
E. Lung KP spheroids were grown under normoxic, hypoxic and 3MIC conditions. Boxplots show GFP fluorescence (hypoxia) relative to mCherry-CAAX levels. Clusters in the 3MIC were grouped into three groups based on their distance from the opening. Representative images of normoxic, hypoxic, and 3MIC conditions. Bars:1000μm,100μm for insets.
F. Lung KP spheroids expressing 5xHRE-GFP and mCherry-CAAX were grown without consumers, or in 3MICs enclosed in glass or PDMS. Points: *per* spheroid GFP (hypoxia) normalized to mCherry-CAAX levels. Lines: linear fit. Panels on the show representative images of spheroids grown under no consumer, glass, and PDMS 3MICs. Bars: 1000μm, 100μm for insets.

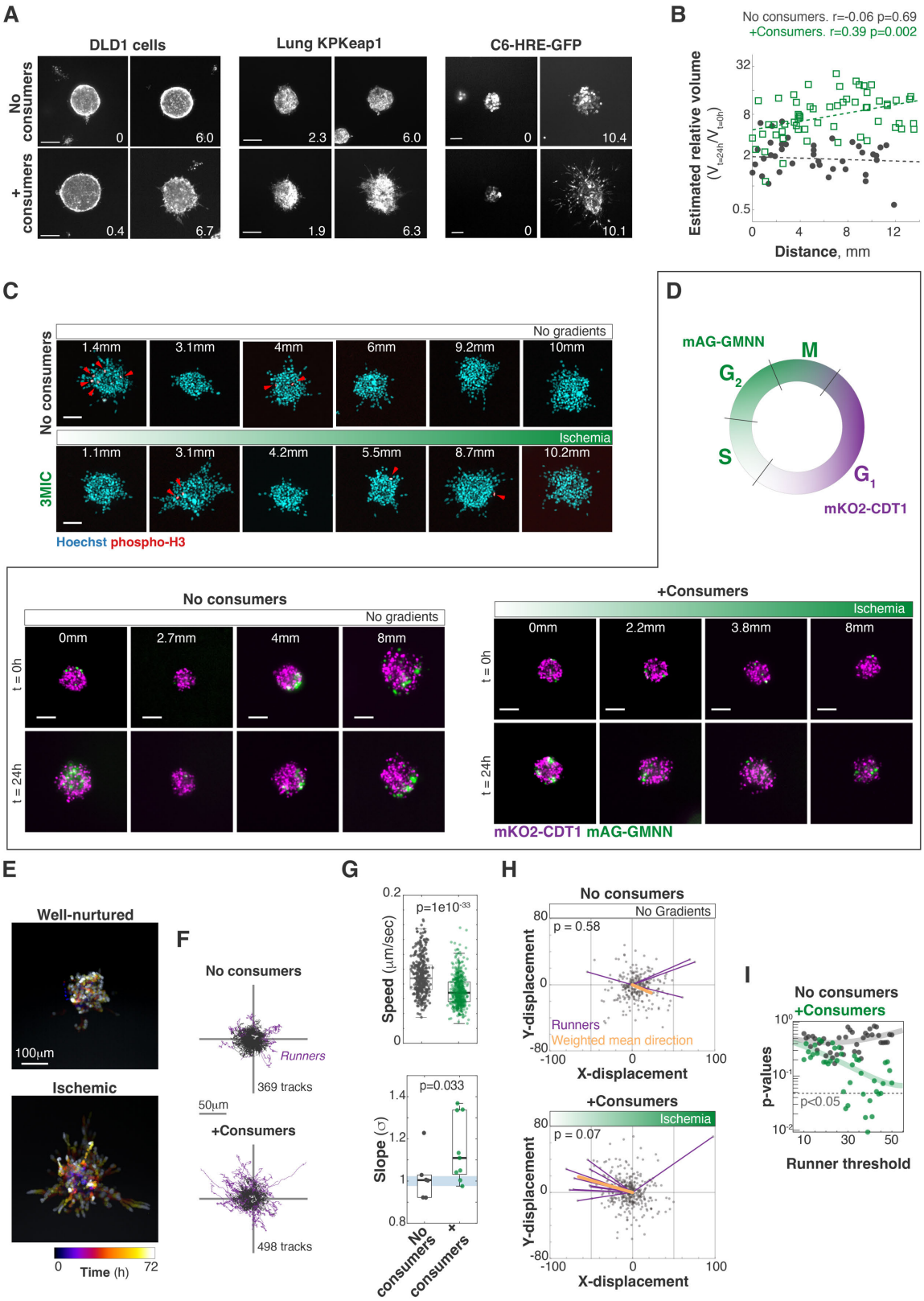
A
DLD1 cells
Lung KPKeap1
C6-HRE-GFP
No consumers
+ consumers
0
6.0
2.3
6.0
0
10.4
0.4
6.7
1.9
6.3
0
10.1
B
No consumers. r=-0.06 p=0.69
+Consumers. r=0.39 p=0.002
Estimated relative volume
(V t=24h/V t=0h)
Distance, mm
C
No gradients
1.4mm
3.1mm
4mm
6mm
9.2mm
10mm
No consumers
Ischemia
1.1mm
3.1mm
4.2mm
5.5mm
8.7mm
10.2mm
3MIC
Hoechst phospho-H3
D
mAG-GMNN
M
G2
S
G1
mKO2-CDT1
No consumers
No gradients
0mm
2.7mm
4mm
8mm
t = 0h
t = 24h
+Consumers
Ischemia
0mm
2.2mm
3.8mm
8mm
mKO2-CDT1 mAG-GMNN
E
Well-nurtured
100μm
Ischemic
0
Time (h)
72
F
No consumers
Runners
369 tracks
50μm
+Consumers
498 tracks
G
p=1e10-33
Speed (μm/sec)
p=0.033
Slope (σ)
No consumers
+ consumers
H
No consumers
No Gradients
p = 0.58
Y-displacement
Runners
Weighted mean direction
X-displacement
+Consumers
Ischemia
p = 0.07
I
No consumers
+Consumers
p-values
p<0.05
Runner threshold

Supplementary Figure 2: Ischemia increases cell motility and invasion

A. Representative images of spheroids of DLD1 cells (colorectal adenocarcinoma cells), $KRAS^{G12D}$ p53-/- Keap1-/- cells (KPKeap1, lung adenocarcinoma) expressing 5xHRE-GFP and C6-hre-GFP cells (rat glioma) grown in 3MICs with or without consumers. Numbers in lower right corner denote the distance to the opening in mm. Bars: 100μm.

B. Quantification of estimated volume change of Lung KP spheroids. Points: area change of individual clusters, lines: linear fit.

C. Phospho-H3 immunofluorescence staining of Lung KP spheroids in 3MICs. Red arrows: Proliferating cells. Bars: 100μm.

D. FUCCI-expressing lung KP clusters stably express mKO2-CDT1 in the G1 cell cycle phase or mAG-GMNN in other phases of the cell cycle. Clusters growing in the absence of ischemic gradients have many proliferating cells throughout the duration of the experiment, whereas ischemic clusters in the 3MIC have progressively lower numbers of proliferating cells, showing a higher portion of cells in G1. Bars: 100μm.

E. Temporal projection of a representative ischemic cluster over a 72h time-lapse.

F. Migratory tracks for all cells tracked in 3MICs and pooled according to the presence or absence of consumers. Tracks of cells that with a net displacement of 50μm or more (runners) are highlighted in magenta.

G. Top: Instantaneous speeds of individual cells in the presence or absence of consumers. Bottom: MSD constants for cells moving in the presence or absence of consumers. Each dote is the MSD constant calculated from multiple tracks within one spheroid.

H. Final position of each tracked cell centered to their origins. Magenta vectors highlight the displacement and direction of runner cells. Vector sum (orange) shows a small bias towards higher nutrient levels in the presence of consumers. However, this bias is only significant (Raleigh-Moore directional test) under some thresholds to define 'runner cells' (**I**).

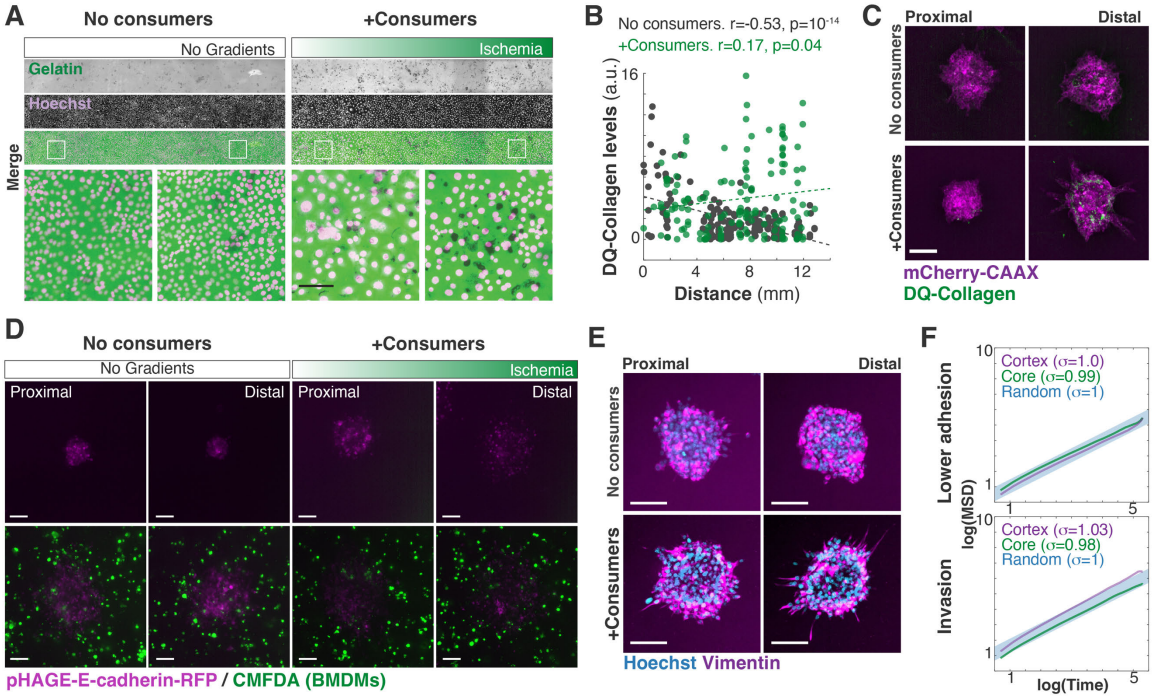

Supplementary Figure 3: Ischemia enhances invasiveness of Lung KP spheroids.

A. Lung KP cells were grown on 488-Gelatin coated coverslips and used as consumers. Increase in degradation of gelatin was observed with increase in distance from the opening in 3MIC, while no significant degradation was observed under no gradient conditions. Bars: 100μm.

B. Quantification of fluorescence intensity of DQ collagen showing a gradual increase in cleaved collagen with increase in distance of the spheroid from the opening. Points: DQ-collagen levels per cluster (GFP-fluorescence intensity normalized to mCherry-CAAX fluorescence). Dashed line: linear fit

C. Representative images of Lung KP spheroids grown on DQ collagen. The distal ischemic spheroids increased their collagen/ECM cleavage. Bars: 100μm.

D. Lung KP tumor spheroids stably expressing pHAGE-E-cadherin-RFP (E-cadherin reporter) were co-cultured with BMDMs. Ischemia and BMDMs have an additive effect in decreasing E-cad levels. Bars: 100μm

E. Representative images of Lung KP spheroids grown in the 3MIC and stained for vimentin. Bars: 100μm.

F. Mean-squared displacement analysis for simulated well-nurtured cells and ischemic cells. Models included lower cell-cell adhesion in ischemia or increased invasion. The synergistic effects of both properties are shown in main figure 3.

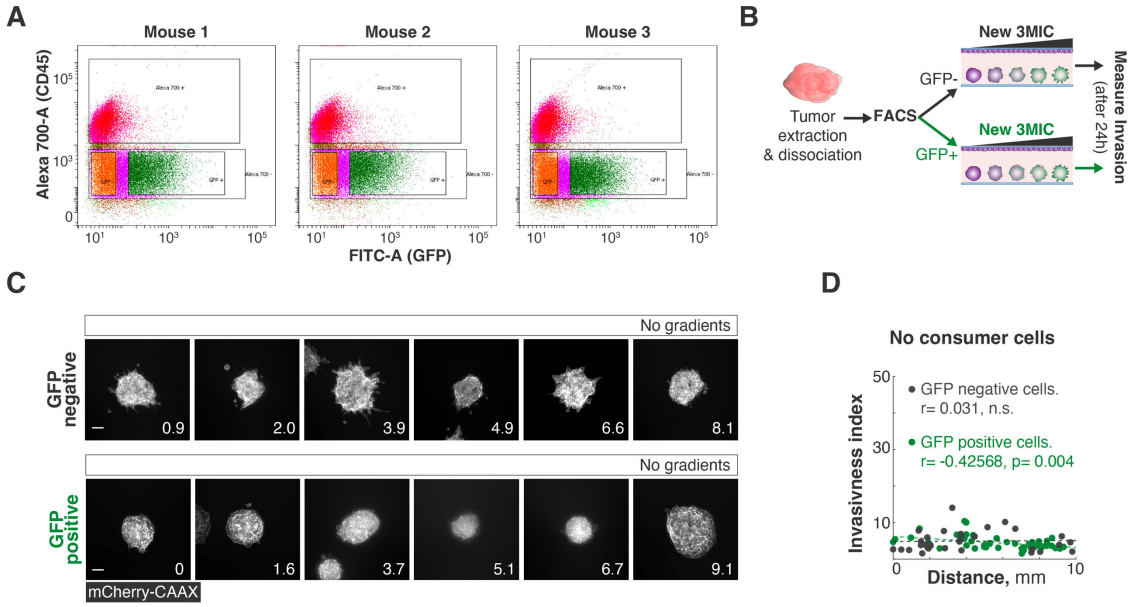

Supplementary Figure 4: Ischemia-induced changes are phenotypic.
A. 3x10^5 Lung KP cells expressing 5xHRE-GFP were injected subcutaneously into the flank of syngenetic mice. Tumors were then dissociated into single cells which were then FACS-separated into GFP+ and GFP- populations. Plots show FACS data for tumor from three different mice.
B. Experimental workflow: Sorted cells were then grown in separate 3MICs with or without consumers.
C. Representative images of spheroids culture in 3MICs with no gradients (no consumers). Bars: 100μm.
D. In the absence of consumers, cells derived from hypoxic tumor regions did not show a significant increase of invasion or motility.

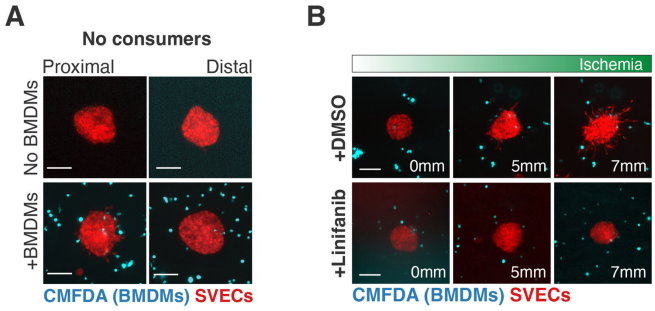

Supplementary Figure 5: Ischemic macrophages induce sprouting of SVEC spheroids.
A. Representative images of SVEC clusters co-cultured with BMDMs in the absence of consumers (no gradients). Under these conditions, little to no sprouting was observed. Bars: 100μm.
B. In the presence of consumers (in this case also SVECs), BMDMs dramatically increase sprouting in SVEC clusters. This effect is abrogated by the VEGFA inhibitor Linifanib. Bars: 100μm.

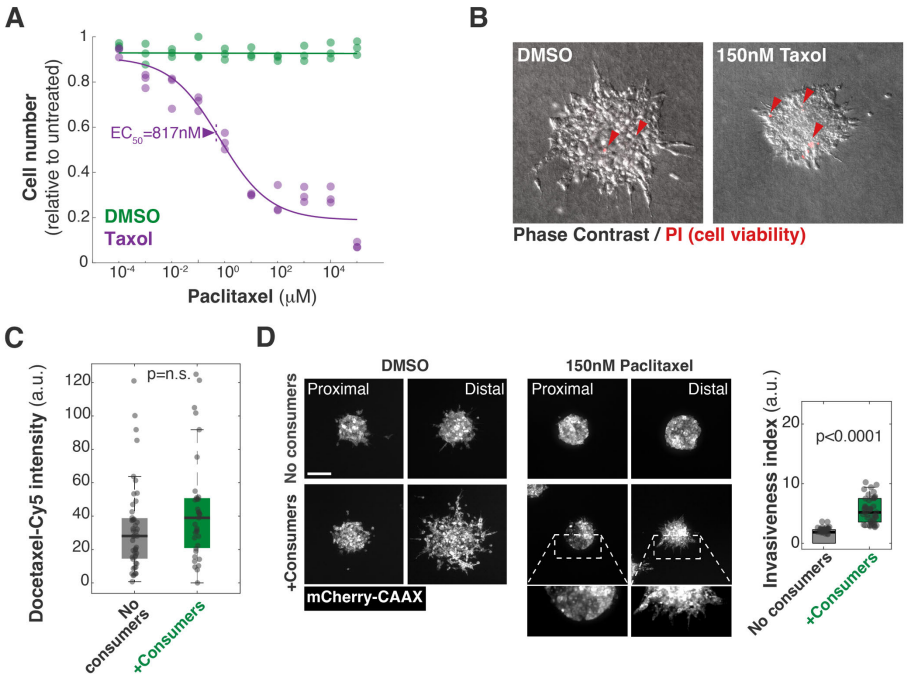

Supplementary Figure 6: Ischemic spheroids are resistant to paclitaxel.

A. Lung KP cells were treated with different doses of paclitaxel for 24 hours. Viability was determined by propidium iodide (PI) incorporation to determine the IC_{50} values.

B. Representative images of Lung KP spheroids showing no significant difference in the number of viable cells in spheroids grown in the 3MIC in the presence or absence of 150nM paclitaxel. Arrowheads: PI positive (non-viable) cells.

C. Boxplot showing that the presence of consumer cells does not decrease Docetaxl-Cy5 levels in spheroids within the 3MIC. Dots: *Per* spheroid Docetaxl-Cy5 levels.

D. Representative images and quantification of Lung KP spheroids treated and untreated with 150mM Paclitaxel. Distal spheroids can invade the ECM even when treated with Paclitaxel but only in the presence of consumers (ischemia). Bars: 100μm.

SUPPLEMENTARY VIDEO LEGENDS

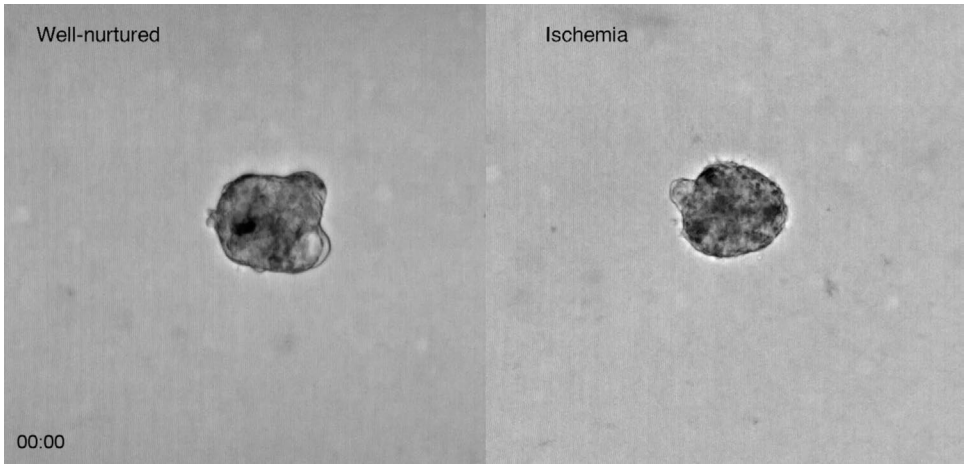

Video S1. Lung KP spheroids grown in 3MIC. Left panel shows spheroid growing close to the opening of 3MIC (well-nourished) and right panel shows a spheroid growing in the ischemic region of 3MIC. Images were acquired every 15 mins for a period of 72 hours.

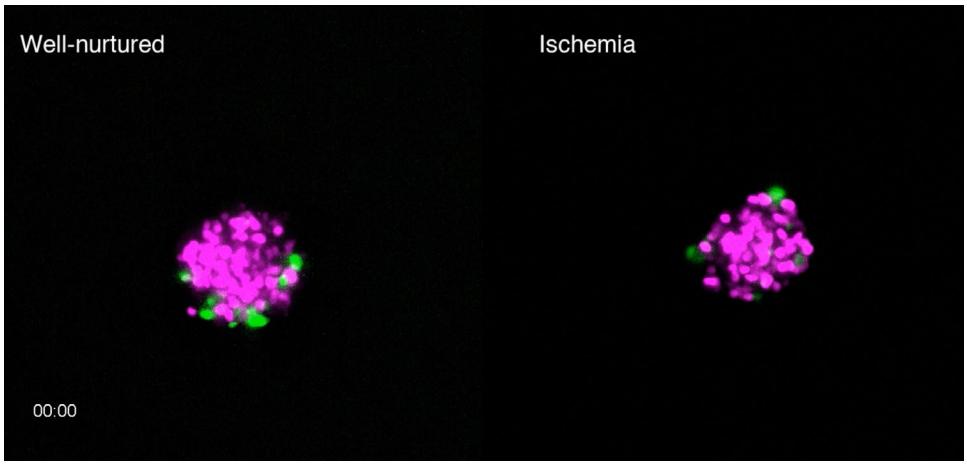

Video S2. Lung KP spheroids stably expressing the pBOB-EF1-FastFUCCI-Puro construct were grown in 3MIC. Movie shows the cell-cycle progression of the cells in the spheroids growing in well-nourished regions (left panel) and ischemic regions (right panel).

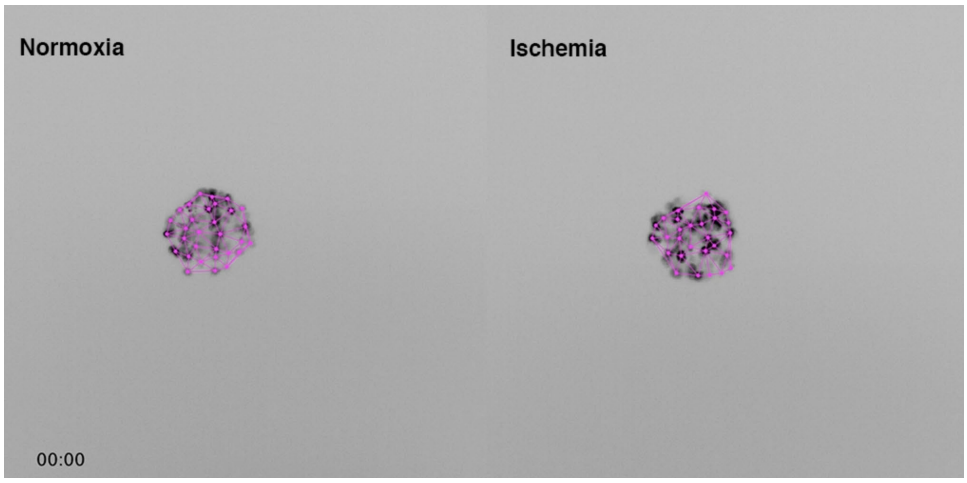

Video S3. Movie depicting the decrease in cell density (or increase of area in between cells). Cells are labelled with H2B-YFP (black). Purple lines show results from Delaunay triangulation algorithm.

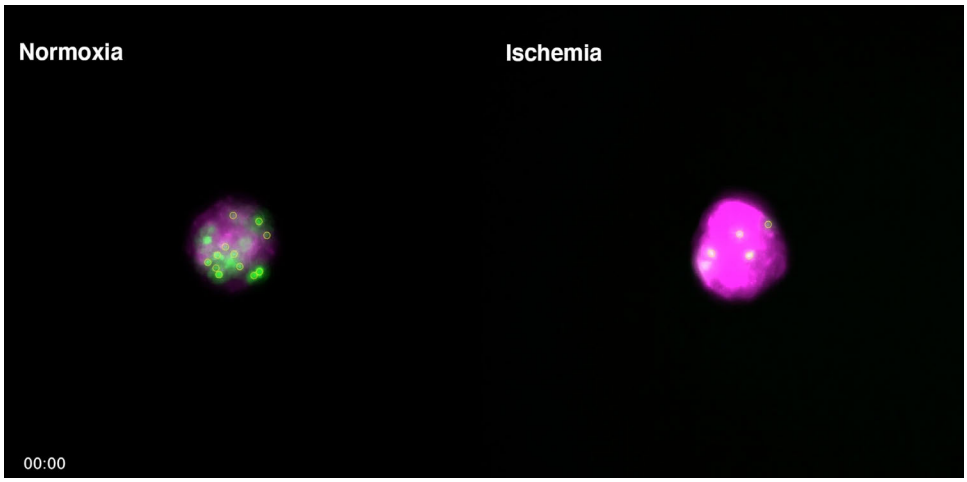

Video S4. Chimeric Lung KP spheroids of cells expressing H2B-YFP (green) or mCherry-CAAX (magenta) mixed at a 1:4 ratio. Time-lapse video shows the migration tracks of H2B-YFP positive cells in spheroids grown in well-nurtured and ischemic regions of 3MIC.

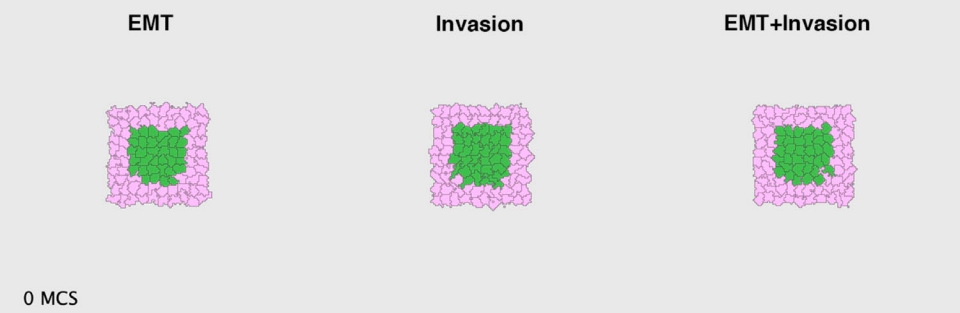

Video S5. Movie depicting the evolution of three Cellular Potts Models simulating the movements of cells arranged as a core of 'ischemic' cells surrounded by cortical, well-nurtured cells. In these models, core cells are assigned a reduced epithelial cell adhesion, increased ECM invasion, or the combination of both using. MCS: Monte Carlo Step (time unit).

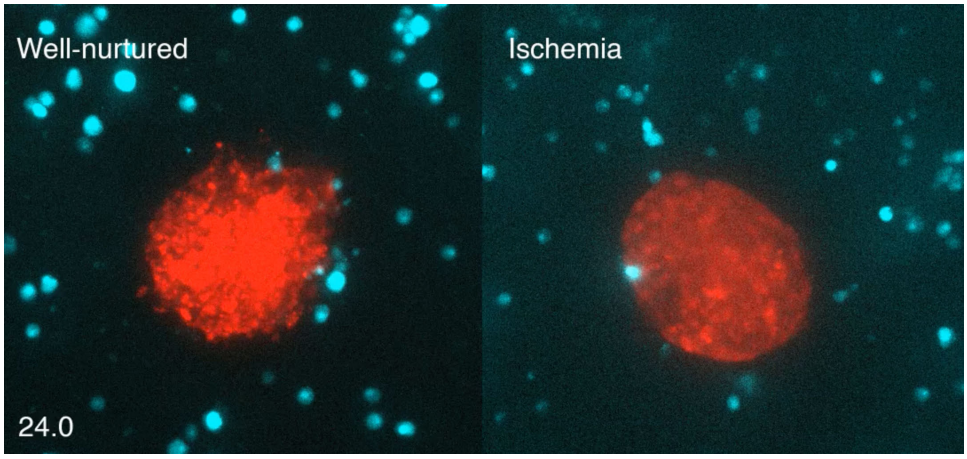

Video S6. Time lapse of SVEC spheroids (expressing mCherry, red), growing in the 3MIC with BMDMs (labelled with CMFDA, cyan) embedded in the ECM. Images were acquired from 24 hours every 30 mins for a period of 72 hours.

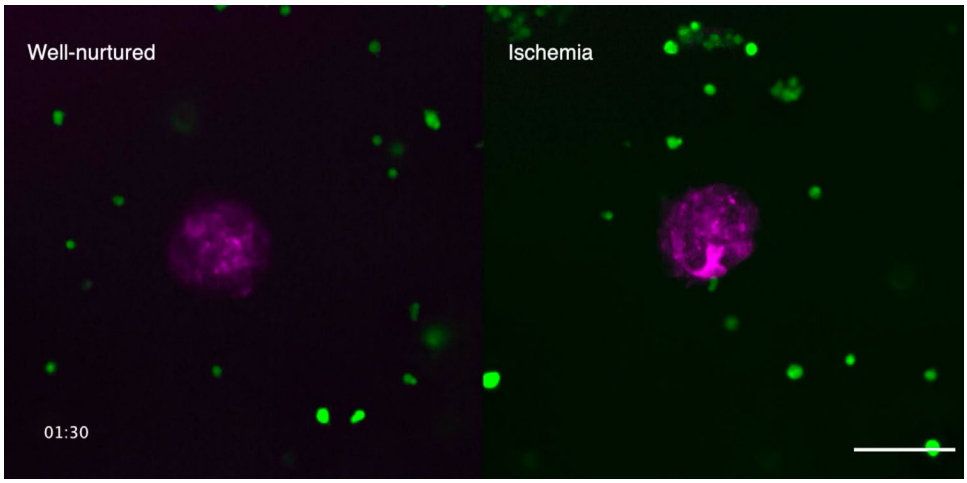

Video S7. Time lapse of Lung KP (expressing mCherry-CAAX, magenta) spheroids growing in 3MIC in the 3MIC with BMDMs (labelled with CMFDA, green) embedded in the ECM. Images were acquired every 30 mins for a period of 72 hours.

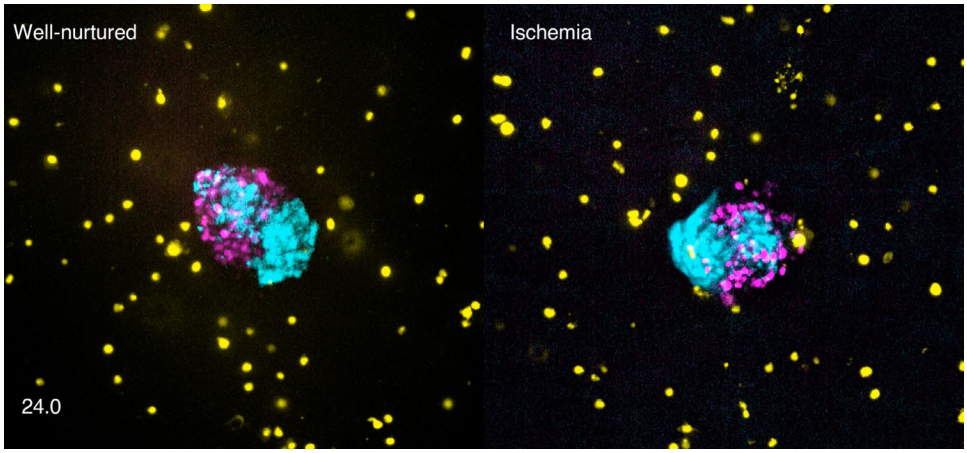

Video S8. Time lapse of spheroids formed by Lung KP cells (magenta) and SVECs (cyan), growing in the 3MIC with BMDMs (yellow) embedded in the ECM. Images were acquired from 24 hours every 30 mins for a period of 66 hours.

SUPPLEMENTARY TABLES

Condition	$J_{C1,C1}$	$J_{C1,C2}$	$J_{C2,C2}$	$J_{C1,ECM}$	$J_{C2,ECM}$
Increased Invasion	16	16	16	2	11
Decreased epithelial adhesion	24	16	8	11	11
Both	24	16	8	2	11

Table S1. CPM parameters for different conditions. $J_{C1,C1}$ is the surface energy between to cells or a cell and the ECM. Higher surface energies lead to lower affinity. C1: core cells. C2: cortical cells. ECM: Substrate (extracellular matrix).

Parameter	Value	Units
Temperature	37	ºC
Population size	100	cells
Target cell size	40	pixels
Dimensions	200x200	pixels
Boundary conditions	Periodic	N/A

Table S2. Additional CPM parameters.